Materials Today Chemistry 41 (2024) 102255

Contents lists available at ScienceDirect

Materials Today Chemistry

journal homepage: www.journals.elsevier.com/materials-today-chemistry/

Molybdate-based double perovskite materials in methane dry reforming

Thomas F. Winterstein [a,1], Christoph Malleier [a,1], Bernhard Klötzer [a], Volker Kahlenberg [b], Clivia Hejny [b], Maged F. Bekheet [c], Julian T. Müller [c], Aleksander Gurlo [c], Marc Heggen [d], Simon Penner [a,*]

[a] Institute of Physical Chemistry, University of Innsbruck, Innrain 52c, A-6020, Innsbruck, Austria
[b] Institute for Mineralogy and Petrography, University of Innsbruck, Innrain 52d, A-6020, Innsbruck, Austria
[c] Technische Universität Berlin, Faculty III Process Sciences, Institute of Materials Science and Technology, Chair of Advanced Ceramic Materials, Straße des 17. Juni 135, 10623, Berlin, Germany
[d] Ernst Ruska-Centre for Microscopy and Spectroscopy with Electrons, Forschungszentrum Jülich GmbH, Leo-Brandt-Str. 1, D-52428, Jülich, Germany

ARTICLE INFO

Keywords:
Double perovskite
Strontium nickel molybdate
Strontium cobalt molybdate
Methane
Activation

ABSTRACT

A series of Sr_2MMoO_6 (M = Ni, Co and (Ni,Co)) compounds was tested as representative model systems to highlight the capabilities of double perovskite structures as precursor materials for methane dry reforming (DRM) applications. Pretreatments in either pure hydrogen or dry reforming CO_2/CH_4 mixtures exclusively yield partial decomposition of the initial double perovskite structures through exsolution of small Ni or CoO particles and the associated formation of additional crystalline compounds, such as $SrMoO_4$ or $SrCO_3$ (in DRM mixtures). The formation of a defective $Sr_{11}Mo_4O_{23}$ transient phase has been revealed by in situ X-ray diffraction measurements in a pure hydrogen atmosphere. The main difference between the Ni- and Co-containing Sr molybdate perovskite structures is the much stronger oxidation propensity of exsolved Co, most likely by oxygen supply from the partially intact double perovskite structure. For Sr_2NiMoO_6, the resulting metallic Ni-double perovskite interface is highly DRM active without strong coking, both if a pre-reduction step in hydrogen is carried out before the DRM experiment or if Sr_2NiMoO_6 is directly decomposed in the DRM mixture. Despite partial decomposition, the corresponding Sr_2CoMoO_6 structure is not active under DRM operation, most likely due to the in situ formation of small exsolved CoO particles, while Ni is exsolved in its metallic state. Different strategies to improve the catalytic activity, including hydrogen by-mixing, enhanced A-site deficiency or co-alloying with Ni have been followed, but only the latter has a beneficial effect on improving the DRM activity at compositions of $Sr_2Ni_{0.5}Co_{0.5}MoO_6$. In $Sr_2Ni_{0.5}Co_{0.5}MoO_6$, the substitution of Co by Ni suppresses the oxidation propensity of Co and during DRM yields the exsolution of Co-rich Ni–Co alloy nanoparticles. We also reveal a strong response of molybdenum as the B' site cation to reduction and DRM treatment, causing the formation of reduced MoO_x phases accompanying the exsolution process.

1. Introduction

The dry reforming of methane (DRM) reaction is a viable way to convert two anthropogenic greenhouse gases, carbon dioxide (CO_2) and methane (CH_4), into a carbon monoxide (CO) and hydrogen (H_2) mixture (so-called "syngas"). The latter can be used as a valuable feedstock for the production of a wide array of synthetic chemicals, including Fischer-Tropsch products, aldehydes or alcohols [1]. The DRM reaction (equation (1)) is highly endothermic ($\Delta H^\circ_{298} = 247.3\ kJ\ mol^{-1}$), which requires operation at elevated temperatures, typically between 600 °C–1000 °C [1].

Methane Dry Reforming:

$$CO_2 + CH_4 \rightarrow 2CO + 2H_2 \quad \text{(eq. 1)}$$

Reverse Water Gas Shift reaction:

$$CO_2(g) + H_2(g) \rightleftharpoons CO\ (g) + H_2O(g) \quad \text{(eq.2)}$$

Steam Reforming of Methane:

$$CH_4(g) + H_2O\ (g) \rightleftharpoons 3H_2(g) + CO(g) \quad \text{(eq. 3)}$$

* Corresponding author.
E-mail address: simon.penner@uibk.ac.at (S. Penner).
[1] These two authors contributed equally.

https://doi.org/10.1016/j.mtchem.2024.102255
Received 21 May 2024; Received in revised form 23 July 2024; Accepted 14 August 2024
Available online 11 September 2024

Boudouard reaction:

$$2CO\ (g) \rightleftharpoons CO_2(g) + C(s) \quad \text{(eq. 4)}$$

Methane decomposition:

$$CH_4(g) \rightleftharpoons 2H_2(g) + C(s) \quad \text{(eq. 5)}$$

The DRM reaction represented by eq. (1) is only the main reaction, which is accompanied by a plethora of side reactions, including methane decomposition, methane steam reforming, Boudouard reaction and/or the water-gas shift equilibrium (eqs. (2)–(5)). All of these reactions are critical for catalyst coking, regeneration, and activity/selectivity [1,2]. The archetypical, most widely used catalyst material is Ni metal. It offers very high activity in both carbon dioxide and methane activation, but suffers from the severe drawback of sintering of the active metal particles and surface/bulk deactivation by coke deposition [3]. To overcome this issue materials-wise, a number of material classes, e.g., complex oxides [2,4] or intermetallic compounds [4,5] have been successfully screened. In many cases, the studied catalyst entities rival or even outperform the archetypical materials in terms of catalyst stability, suppression of coke formation or catalyst activity [1–5]. A particularly promising class of materials is perovskites, which feature the general formula ABX_3, where X is usually a halide or oxygen and A and B are typically bi- or trivalent ions occupying the dodecahedrally and octahedrally coordinated sites. Typical A site ions are earth-alkaline metal ions (e.g., Sr^{2+} or Ca^{2+}) or other large cations such as La^{3+}. The B site ions are usually transition metal ions [2]. The huge advantage of perovskites is the possibility to tune the structural and physico-chemical properties of the materials by an adequate choice of the A- and B-site ions [2]. This likewise affects the oxygen vacancy concentration/oxygen mobility, structural stability or catalytic activity/selectivity [2]. These beneficial properties also hold for so-called double perovskite structures, which are characterized by the general formula $AA'BB'O_6$. The characteristics of this class of materials are the appearance of different possibilities of B-site cation ordering, such as rock-salt, layered or columnar [6]. The ordering phenomena directly affects the crystal chemistry of the materials and the possibility of valence mixing at the B/B′ site gives rise to an even more pronounced tuning of catalytic, structural or electronic properties. Consequently, double perovskites can be formed by successive substitution of A′ for A and/or B′ for B. This initially leads to a doped single perovskite $A_{1-x}A_x'BO_3$ (or $AB_{1-y}B_y'O_3$), where in general, the cations adopt a disordered structure through random occupation of the A- or B-sites. If A and A (or B′ and B) differ significantly in size or charge, and x (or y) is approximately equal to 0.5, ordered double perovskites may be formed. It is worth noting that the important benefits are significantly improved compared to their single perovskite counterparts. These include (i) the expansion of the compositional space because double perovskite structures may accommodate elements/ions that cannot exist in standard perovskites (e.g., high valence states +6 or +7), (ii) the complex atomic coordination can lead to electronic structures not found in standard perovskites and (iii) double perovskites can exhibit a higher chemical stability, e.g., in highly reducing or oxidizing environments [7].

The use of (double) perovskites in the DRM reaction is usually connected to the exploitation of perovskite structures as precursors, which are decomposed in a controlled manner to result in well-distributed metal nanoparticles embedded in an oxide matrix. The formation of the metal-oxide interface gives rise to a bifunctional catalytic mechanism, in which the metal (methane activation) and oxide (carbon dioxide activation) share duties. This mechanism is prevalent in the most studied $LaNiO_3$ and La_2NiO_4 materials, where $La_2O_2CO_3$ (as a result of perovskite decomposition towards La_2O_3) is reversibly formed and decomposed by CO_2 activation and release [8,9]. Recent studies have also shown that even interfacial carbides can act as a reactive intermediate [10,11]. This interface features higher structural and sinter stability with enhanced catalytic activity and suppressed carbon deposition. Perovskite decomposition necessarily goes along with the exsolution of metal particles from the (double) perovskite lattice and is such a common phenomenon [12,13]. It is usually induced by a separate pre-reduction step (mostly in hydrogen) or "in situ" in the reaction mixture itself. While the exsolution of metals from several single perovskites, especially for DRM applications, has already been scrutinized especially for DRM applications [5,8,14–16], much less information is available for double perovskites as starting precursors. To date, research on double perovskites has focused primarily on the exsolution of iron, iron-nickel, and cobalt-iron alloy particles from (cobalt-doped) $Sr_2Fe_{1-x}Mo_xO_6$ and $Sr_2Ni_xFe_{1-x}O_6$ materials [17–25]. A composition-dependent $FeNi_3$ exsolution, correlated with increased CO_2 and CH_4 conversion, has been found. Molybdate-based double perovskites with Sr on the A site exhibit especially excellent exsolution properties [17]. The formation of a Mo^{6+}/Mo^{5+} redox couple upon reduction is of particular importance in the context of DRM applications, specifically in the case of Sr_2NiMoO_6 and Sr_2CoMoO_6. This redox couple enhances the dissociative chemisorption of methane, which is a crucial step in the overall process. In due course, the formation of Mo═O species is reported to favor the reaction of methane with a surface ion by lowering its acidity and desorption energy for the oxidized reaction product [26].

It is noteworthy that, despite the information that has been compiled so far, ex situ post-mortem catalyst characterization is typically the only available data for such double perovskites in DRM. This represents a significant limitation, as analogous studies on single perovskites, particularly pure and doped $LaNiO_3$, have demonstrated that the characterization of the spent catalyst state is insufficient to draw definitive conclusions about the active site. Structural transformations occurring during DRM operation tremendously influence the catalytic properties, and include the formation of oxygen-deficient phases, Ruddlesden-Popper phases or oxy-carbonates [8]. The objective of the present study is to examine the reductive stability and associated DRM properties of two "model" double perovskite structures, Sr_2NiMoO_6 and Sr_2CoMoO_6. Both double perovskite structures have been selected, as the corresponding Ni- and Co-containing perovskites have already shown prospective methane activation and DRM properties [8,15]. The use of Ni- and Co-based double perovskites on molybdate basis also allows us to eventually connect the exsolution properties of the B-site ion (Ni, Co) with possible changes in the electronic structure and oxidation state of the B' ion (Mo) and their effects on DRM activity. In due course, we will compare the eventual transition of the double perovskite precursor structure into the metal/oxide/perovskite composite in hydrogen and in the DRM reaction mixture, as for single perovskites, distinct differences in the observed transient structures and Ni particle sizes have already been obtained. The cross-correlation of the Ni- and Co results will yield similarities and differences in the stability, decomposition route, carbon resistance, and oxidation behavior of the exsolved metal particles in double perovskite. Additionally, activation strategies for selected Sr_2CoMoO_6 materials, including A-site deficiency and co-alloying of Co with Ni, will be discussed.

2. Experimental

2.1. Synthesis of Sr_2NiMoO_6, Sr_2CoMoO_6, $Sr_2Ni_xCo_{1-x}MoO_6$ and $Sr_{1.9}CoMoO_6$

For synthesis of the double perovskite materials Sr_2NiMoO_6, Sr_2CoMoO_6, $Sr_2Ni_{0.1}Co_{0.9}MoO_6$ and $Sr_2Ni_{0.5}Co_{0.5}MoO_6$ and $Sr_{1.9}CoMoO_6$ we followed a solid-state preparation route, which includes mechanically mixing the starting materials $SrCO_3$ (Sigma-Aldrich, 99.9 % trace metals basis), Co_3O_4 (Thermo Fisher, 99.7 % metals basis), NiO (Thermo Fisher, Puratronic 99.998 % metals basis) and MoO_3 (Thermo Fisher, 99.95 % metals basis) in the respective nominal stoichiometries followed by grinding and homogenizing the powders in ethanol with an agate ball mill at 600 rpm for 45 min. After evaporation of the alcohol, the powder was calcined at 900 °C for 24 h, after which it was ground and pressed

into a pellet. The pellets were subsequently subjected to repeated sintering – grinding cycles, including heating to 1350 °C for 24 h followed by re-pelletizing into a tablet of 10 mm diameter and 0.8 mm thickness. This procedure was repeated until X-ray diffraction (XRD) indicated the lowest achievable amount of parasitic structures. The amounts used for the synthesis of 2 g material each are summarized in Table 1.

For Mo-based double perovskite structures, a very low amount of $SrMoO_4$ (<3 wt.-%) is always observed. This compound is isotypic with zircon ($ZrSiO_4$). As will be shown in this contribution, the appearance/formation and transformation into other Sr-molybdate structures are highly dynamic and strongly dependent on the gas atmosphere and treatment. The synthesis of all the compounds yielded a double perovskite structure. Fig. 1 shows a representative tetragonal crystal structure of Sr_2NiMoO_6.

2.2. Structural and spectroscopic characterization

Ex situ structural analysis of benchmark materials after selected treatments was carried out using a Rigaku SmartLab-SE instrument in focused beam setting and reflection mode (Co-Kα, λ = 1.7890 Å) using a D/teX Ultra 250 compound silicon strip 1D-detector (Rigaku, Tokyo, Japan). The ground sample was placed on a glass-sample holder, and the patterns were recorded in a range of 2θ = 10°–90° with a step width of 0.01°.

In situ synchrotron-based PXRD experiments have been conducted on both DRM mixtures under pure hydrogen at beamline 12.2.2, Advanced Light Source (ALS) at Lawrence Berkeley National Laboratory, in a cell previously described in Refs. [29,30]. All diffraction patterns were measured in angle-dispersive transmission mode with a focussed 25 keV monochromatic beam (λ = 0.4984 Å/30 μm spot size). The powders were heated in a 0.7 mm outer diameter quartz capillary under quasi-flowing conditions (CH_4: CO_2 = 1:1, gas flow: 1 mL min^{-1} for DRM; pure hydrogen, gas flow 1 mL min^{-1}, GHSV = 600 000 N mL h^{-1} $gcat^{-1}$). Heating was performed using a SiC furnace with an infrared light source up to 800 °C at a rate of 10 °C min^{-1}. All gases were injected through a 0.5 mm outer diameter tungsten tube [29,30]. The program TOPAS 5.0 by Bruker was utilized to analyze the X-ray diffraction patterns using Rietveld refinement with a full axial model [31]. A Double-Voigt approach was applied to calculate the crystallite sizes. The resolution function of the diffractometers was obtained from the structure refinement of a LaB_6 standard.

Surface chemical analysis was carried out in a commercial UHV system for in situ XPS applications (SPECS GmbH). The UHV chamber is comprised of a μFOCUS 600 monochromatic small spot (100 × 300 $μm^2$) Al $K_α$ X-ray source, a hemispherical energy analyzer (PHOBIOS 150 NAP) in a vertical configuration, and a μ-metal analyzing chamber, shielding the system from external magnetic fields. To investigate polycrystalline samples, a pressed pellet covering a stainless-steel grid as a stabilizer is fixed on a sample-holder by mounting the pellet via a front plate. The excited photo-electrons were collected by a 300 μm nozzle directly from the sample's frontside surface via an 8 mm opening in the front plate. Details of the apparatus are given in Ref. [32]. Qualitative analysis was based on the Ni 2p, Sr 2p, Co 2p, O 1s, C 1s and Mo 3d high-resolution spectra. Chemical shifts were calibrated to the signal of the adventitious carbon component at 284.5 eV. Fitting of the Ni 2p, Co 2p and Mo 3d spectra by different components and oxidation states was performed using literature-reported constraints for the full-width at half maximum and the binding energies. Background correction has been done using Shirley- and Tougaard-type functions.

Table 1
Stochiometric masses of reactants used for the perovskite synthesis. The combined mass of each sample is set to 2 g.

Phase	$SrCO_3$ [g]	MoO_3 [g]	NiO [g]	Co_3O_4 [g]
Sr_2NiMoO_6	1.1491	0.5602	0.2907	–
Sr_2CoMoO_6	1.1368	0.5542	–	0.3090
$Sr_2Ni_{0.5}Co_{0.5}MoO_6$	1.1429	0.5572	0.1446	0.1554
$Sr_{1.9}CoMoO_6$	1.1115	0.5704	–	0.3181
$Sr_2Co_{0.9}Ni_{0.1}MoO_6$	1.1380	0.5548	0.0288	0.2784

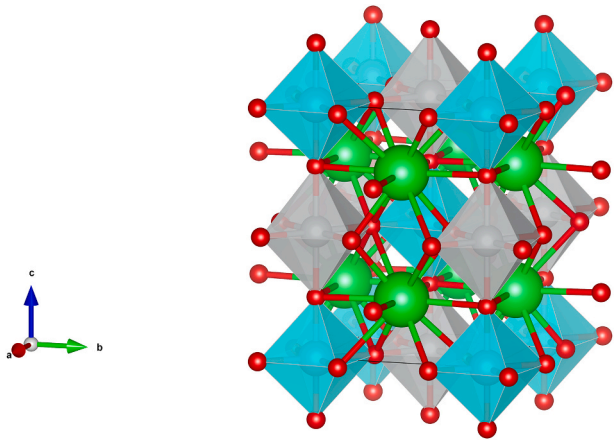

Fig. 1. Structure model of the synthesized representative tetragonal Sr_2NiMoO_6 double perovskite structure. Sr is shown in green, Ni octahedrons in blue, Mo octahedrons in grey and oxygen in red. The graphical illustration was created using the program VESTA [27]. Modelled after the structure described in [28]

Scanning transmission electron microscopy (TEM) characterization via high-angle annular dark field (HAADF) imaging and Energy-dispersive X-ray analysis was carried out on an C_s-aberration corrected (Ceos DCOR) FEI Titan G2 80–200 ChemiSTEM electron microscope operated at 200 kV at the Ernst Ruska-Centre Jülich employing an in-column Super-X energy dispersive X-ray spectroscopy (EDX) unit (ChemiSTEM technology)

2.3. Catalytic characterization

200 mg of sample powder was fixed with quartz wool in a home-built 7 mm (inner diameter) quartz tube flow reactor setup under a total continuous gas flow of 60 mL min^{-1} (CH_4:CO_2:He = 1:1:1 mL min^{-1}). The reactor was heated with 5 °C min^{-1} to 800 °C, followed by an isothermal period at 800 °C for 30 min. An external S-type thermocouple was placed in close contact to the reactor tube to ensure the correct temperature reading. Moreover, an independent calibration of a potential temperature gradient between the external thermocouple and the exact location of the catalyst bed was performed by inserting a second thermocouple into the gas flowing inside the reactor tube. The output gas was directly detected by an on-line quadrupole mass spectrometer (Balzers QME 125). CO_2, CH_4, CO and H_2 were measured at their respective m/z ratios of m/z = 44, 16, 28 and 2, respectively. Relevant fragmentation patterns have been considered. For the display of the catalytic data, we show the conversion of the relevant signals as a qualitative measure of the catalytic activity, as due to the ongoing structural transformations during the DRM reaction, active-site-normalized reaction rates (and consequently, TOF values) cannot be reliably calculated.

3. Results and discussion

3.1. Bulk structure characterization of selected benchmark states of Sr_2NiMoO_6, Sr_2CoMoO_6 and $Sr_2Ni_xCo_{1-x}MoO_6$ before and after hydrogen reduction and methane dry reforming

Figs. 2 and 3 show a combined ex situ PXRD analysis of the as-calcined and differently pre-treated Sr_2NiMoO_6, Sr_2CoMoO_6 and $Sr_2Ni_xCo_{1-x}MoO_6$ samples. These measurements serve as the basis for Rietveld analysis to confirm the presence of the double perovskite

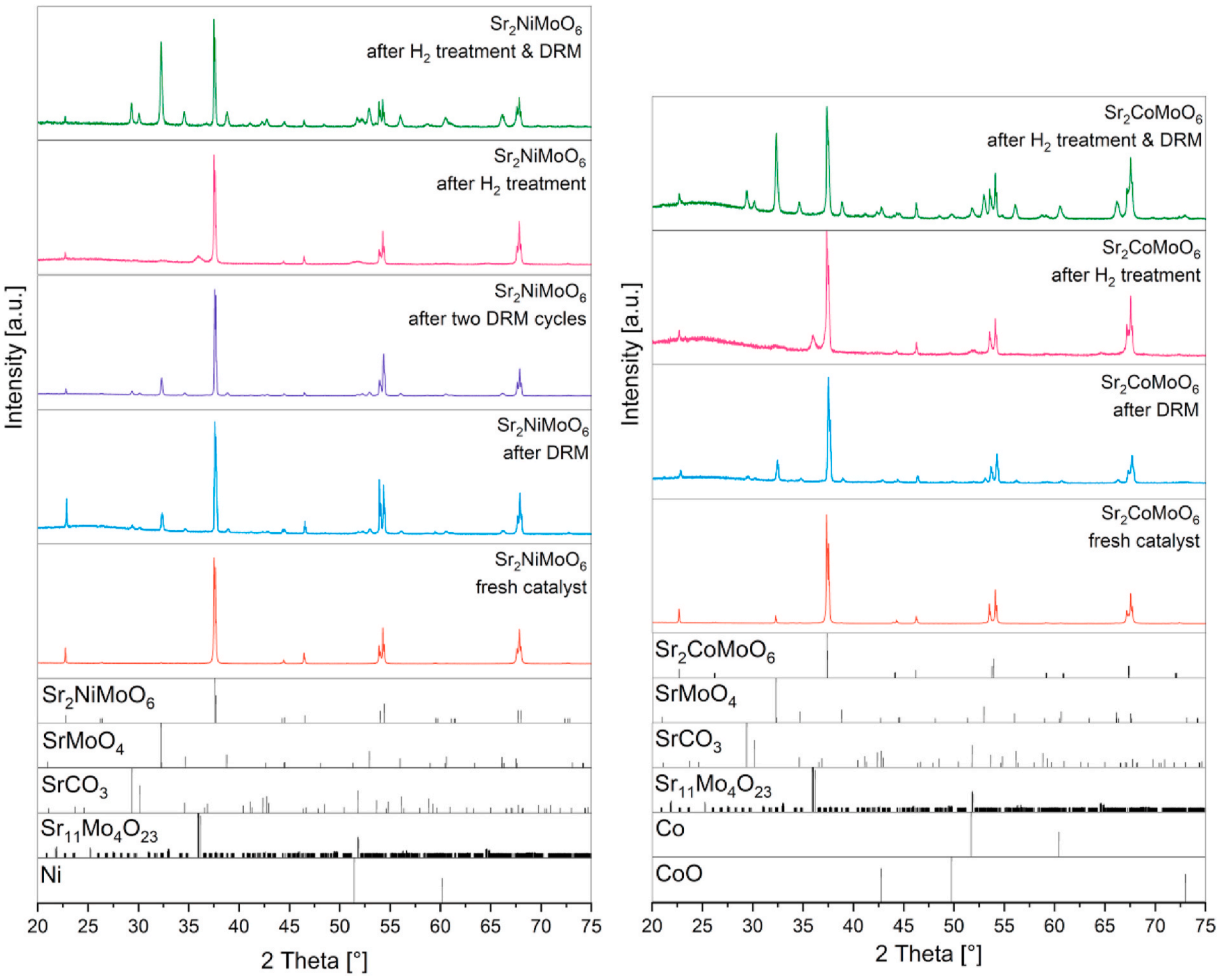

Fig. 2. PXRD analysis of Sr_2NiMoO_6 (Left column) and Sr_2CoMoO_6 (Right column) in the as-calcined state, after pre-reduction in hydrogen at 800 °C, and after one or several DRM cycles up to 800 °C, with and without pre-reduction in hydrogen at 800 °C. Structural references are shown as bars at the bottom of the respective panels. Pattern numbers: Sr_2NiMoO_6 155732 [28], Sr_2CoMoO_6 181514 [33], $SrMoO_4$ 2300460 [34], $SrCO_3$ 9013802 [35], $Sr_{11}Mo_4O_{23}$ 143701 [36], Ni 37502 [37], Co 136039 [38], CoO 9865 [39]. Parameters: Hydrogen or DRM atmosphere (CO_2:CH_4:He = 1:1:1), flow rate: 60 mL min^{-1}, heating rate: 5 °C min^{-1}.

structure and structural benchmarks after different treatments that form the basis of the stability tests discussed in the subsequent section. We were able to synthesize all materials as tetragonal double perovskites with only minor differences in the unit-cell parameters (Table 2). $SrMoO_4$ as the common parasitic phase is present in very low concentrations (i.e., <3 wt.-% for Sr_2CoMoO_6, <2 wt.-% for Sr_2NiMoO_6 and $Sr_2Ni_{0.5}Co_{0.5}MoO_6$ materials). An exception is the $Sr_2Ni_{0.1}Co_{0.9}MoO_6$ sample, which also contains a small $Sr_{11}Mo_4O_{23}$ impurity.

The morphology and chemical homogeneity of all samples were determined by electron microscopy analysis. Fig. 4 shows the results for the calcined Sr_2NiMoO_6 (Panel A) and the $Sr_2Co_{0.5}Ni_{0.5}MoO_6$ (Panel B) samples. In both cases, HAADF images reveal a platelet-like morphology with individual plate sizes of several hundreds of nm. Most importantly, the EDX analysis shows that all elements are homogeneously distributed and no agglomeration of any element occurred.

3.2. Stability of Sr_2NiMoO_6 and Sr_2CoMoO_6 under reduction and methane dry reforming conditions

3.2.1. Structural benchmark states after hydrogen reduction and DRM treatment

With respect to stability, Sr_2NiMoO_6 was already tested in literature [26,40–42] and, although there are contradictory reports on the extent of decomposition, there is common agreement that upon heating in hydrogen/inert gas mixtures, partial or complete decomposition has been observed. Heating in a 5 % H_2/N_2 mixture at 1200 °C yielded exsolution of Ni particles from the double perovskite lattice, essentially resulting in a Ni metal - double perovskite interface with Sr-molybdate parasitic structures [26]. In contrast, heating in 5 % H_2/Ar at 1200 °C yielded complete decomposition into Ni, Sr_3MoO_6, $SrMoO_3$ and $SrMoO_4$ [26]. The latter phase is a common product of the decomposition of Sr–Mo perovskite phases [43]. Of equal importance for DRM applications, Sr_2NiMoO_6 yields partial decomposition into $SrCO_3$, Ni and $SrMoO_4$ in pure CO_2 starting at 600 °C. Ni particles exsolved from Sr_2NiMoO_6 are reported to be highly active in methane activation, leading to strong carbon deposition. Complementary reduction studies for Sr_2CoMoO_6 indicated a similar instability in 5 % H_2–Ar mixtures, with the formation of Sr_3MoO_6 and Co metal at and above 900 °C [43–49]. Also, in pure CO_2, partial decomposition into $SrCO_3$, $SrMoO_4$ and CoO was reported [45].

In our experiments, we generally observe a very high stability in the double perovskite structure, invariant of the gas atmosphere. Table 3 summarizes the phases, weight fractions, and changes in lattice parameters derived from the Rietveld refinement of the PXRD patterns shown in Figs. 2 and 3 for selected treatments. As a general introductory remark, we note that after either reduction treatment in H_2 or CO_2/CH_4, a still intact Ni or Co (CoO)-mixed oxide-double perovskite interface partially prevails at varying extents.

With respect to the stability of Sr_2NiMoO_6, treatments in 1 bar flowing hydrogen at 800 °C (Fig. 2, Panel A) indicate a high stability of

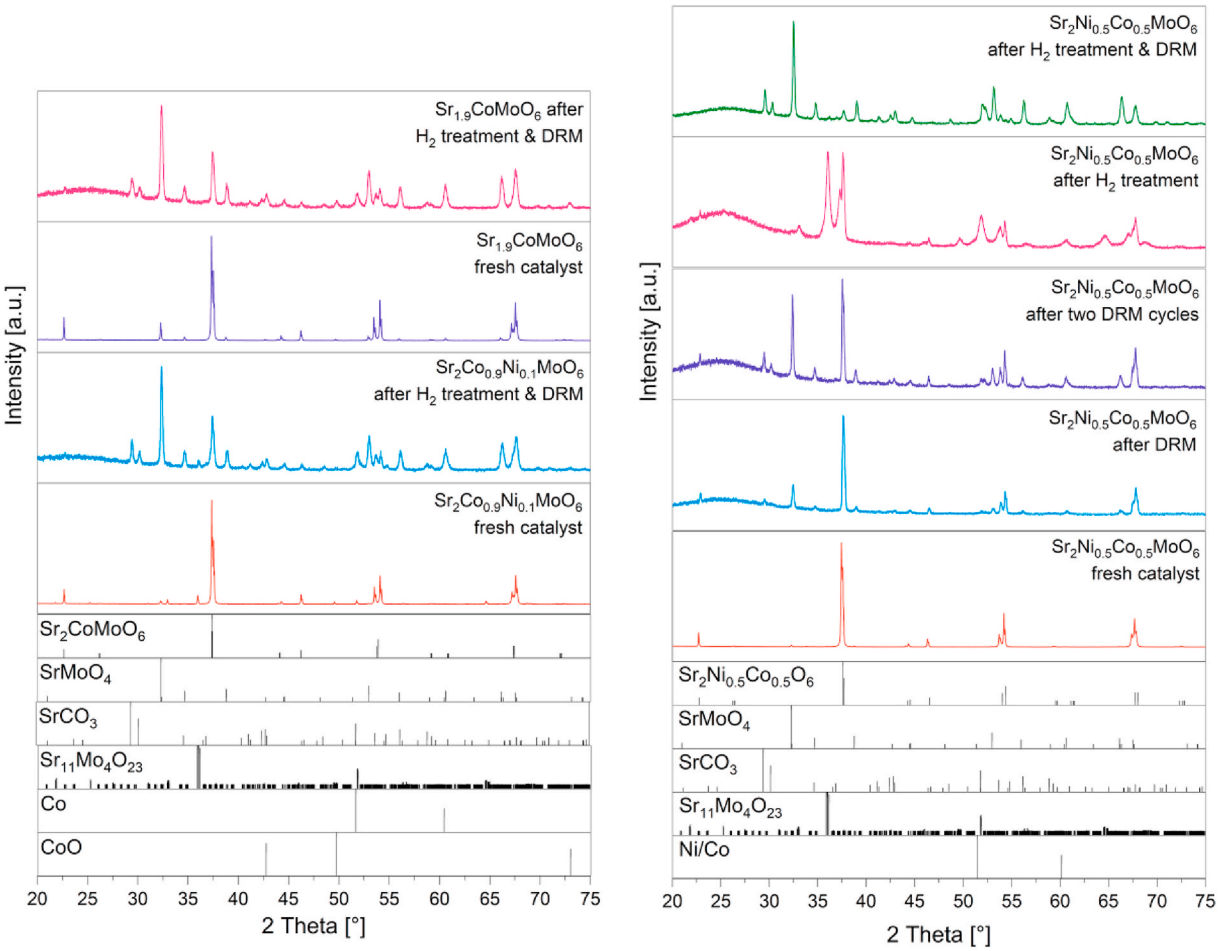

Fig. 3. PXRD patterns collected on A-site deficient and Ni-doped Sr_2CoMoO_6 samples. *Left column*, two top-most panels: A-site deficient $Sr_{1.9}CoMoO_6$ before and after hydrogen treatment at 800 °C followed by a DRM treatment up to 800 °C. Two bottom-most panels: Ni–Co co-doped $Sr_2Co_{0.9}Ni_{0.1}MoO_6$ before and after hydrogen treatment at 800 °C followed by a DRM treatment up to 800 °C. *Right column*: Ni–Co co-doped $Sr_2Co_{0.5}Ni_{0.5}MoO_6$ before and after hydrogen treatment at 800 °C followed by a DRM treatment up to 800 °C and after one or two DRM treatments up to 800 °C without hydrogen pre-reduction. Parameters: Hydrogen or DRM atmosphere (CO_2:CH_4:He = 1:1:1), flow rate: 60 mL min^{-1}, heating rate: 5 °C min^{-1}.

Table 2
Structure and unit-cell parameters of the different double perovskites after 48 h of sintering.

Sample	Structure [Space group]	Weight Fraction [wt.-%]	Cell parameters a [Å]	c [Å]
Sr_2NiMoO_6	Sr_2NiMoO_6 [*I4/m*]	98.9	5.5479	7.8957
	$SrMoO_4$ [$I4_1/a$]	1.1	5.3955	12.0199
Sr_2CoMoO_6	Sr_2CoMoO_6 [*I4/m*]	97.4	5.5676	7.9533
	$SrMoO_4$ [$I4_1/a$]	2.6	5.3955	12.0315
$Sr_2Ni_{0.5}Co_{0.5}MoO_6$	$Sr_2Ni_{0.5}Co_{0.5}MoO_6$ [*I4/m*]	98,6	5.5549	7.9166
	$SrMoO_4$ [$I4_1/a$]	1.4	5.3905	12.0353

the double perovskite with only a minor amount of exsolved Ni particles (10.3 wt.-%). In the ex situ collected PXRD patterns after the hydrogen reduction, two features are worth noting, which will be in turn corroborated by the in situ measurements: first, the parasitic $SrMoO_4$ structure, present after calcination, has vanished, and second, $Sr_{11}Mo_4O_{23}$ appears as an additional phase. Striking is the fact that the latter exhibits a remarkably small crystallite size. $Sr_{11}Mo_4O_{23}$ is reported by Miranda et al. to be a strongly oxygen-deficient cubic double perovskite phase, whose thermodynamic stability strongly depends on the synthesis temperature [36]. Samples synthesized at temperatures lower than 1400 °C inevitably transform to $SrMoO_4$ upon annealing [36]. We corroborate this finding, as the presence of $Sr_{11}Mo_4O_{23}$ (in mind that the temperature did not exceed 800 °C) is extremely sensitive to the reduction potential of the gas atmosphere. Whenever Sr_2NiMoO_6 is exposed to a DRM mixture without hydrogen pre-reduction or a DRM treatment is performed after a hydrogen pre-reduction, the formation of $Sr_{11}Mo_4O_{23}$ is either suppressed or $Sr_{11}Mo_4O_{23}$ is removed by formation of additional $SrMoO_4$. The process of this transformation is further discussed in the context of the in situ PXRD experiments. However, to the best of our knowledge, we report it for the first time as a decomposition product of any strontium molybdate phase during reduction or catalytic treatments. After one and two DRM cycles, respectively, we observe that direct decomposition in a DRM mixture without prior pre-reduction yields a much higher amount of $SrMoO_4$ compared to the calcined state and that the mixture composition hardly changes between the first and the second DRM cycle. The highest amount of $SrMoO_4$ is observed after a hydrogen pre-reduction – DRM cycle. We will show in the in situ PXRD section that this is essentially due to the $Sr_{11}Mo_4O_{23}$ – $SrMoO_4$ intertransformation. Formation of Ni particles by exsolution in the DRM mixture has also been observed, although suppressed compared to after hydrogen reduction (3 wt.-% vs. 10 wt.-%). $SrCO_3$ is also observed in small amounts (ca. 10 wt.-%), which is common for decomposed Sr-containing perovskites in DRM. Finally, the decomposition of Sr_2NiMoO_6 is most pronounced by a pre-reduction step in hydrogen before a DRM experiment. Consequently, the amounts of $SrMoO_4$, $SrCO_3$ and exsolved Ni particles are highest in comparison to all other treatments.

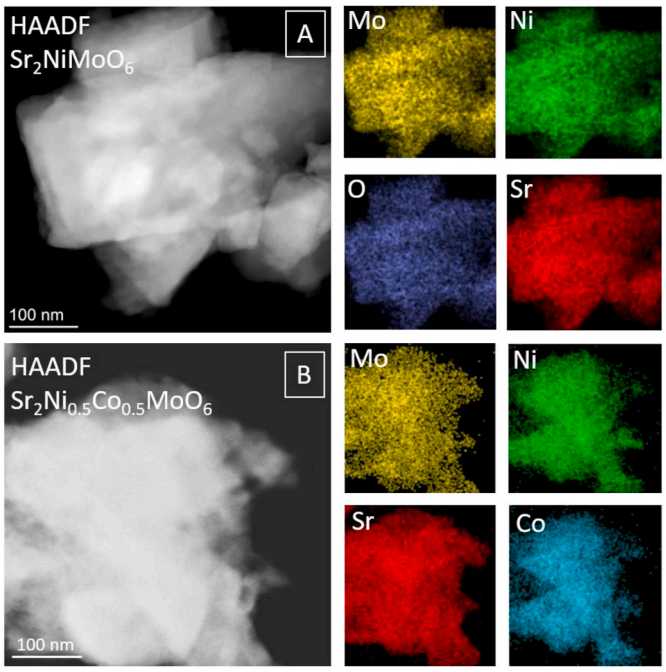

Fig. 4. HAADF images and set of individual EDX maps (Mo–K, Ni–K, Co–K, O–K and Sr–K edges) for the Sr_2NiMoO_6 (Panel A) and the $Sr_2Ni_{0.5}Co_{0.5}MoO_6$ sample (Panel B).

This feature is corroborated by both TEM measurements and the catalytic experiments discussed in the subsequent sections.

The qualitative trends upon treating Sr_2CoMoO_6 in hydrogen and during DRM in terms of phase formation are comparable to Sr_2NiMoO_6. One notable exception, which is at the core of the interpretation of the catalytic results in section 3.3., is that although metallic Co is detected after the hydrogen pre-reduction, DRM treatments either directly or after a pre-reduction without exception lead to the formation of CoO. This is again confirmed by TEM, the suppressed catalytic DRM activity (cf. section 3.3.) and also the XP spectra discussed below.

In accordance with the interpretation of the catalytic results based on the eventual activation of Sr_2CoMoO_6 catalysts, the $Sr_{1.9}CoMoO_6$, $Sr_2Co_{0.9}Ni_{0.1}MoO_6$, and $Sr_2Ni_{0.5}Co_{0.5}MoO_6$ materials were subjected to similar treatments (Fig. 3). In general, the structural behavior after hydrogen reduction and DRM treatments is very much comparable to pure Sr_2CoMoO_6 or Sr_2NiMoO_6. Two notable exceptions are connected to the $Sr_{11}Mo_4O_{23}$ phase: the latter appears already in the calcined state of $Sr_2Co_{0.9}Ni_{0.1}MoO_6$, but not in that of $Sr_{1.9}CoMoO_6$. As the formation of $Sr_{11}Mo_4O_{23}$ depends on the availabilty of additional Sr^{2+} cations (formally, the base structure of $Sr_{11}Mo_4O_{23}$ is close to $Sr_3Mo^{6+}O_6$, i.e., referenced to the starting structure $Sr_2M^{2+}MoO_6$ either Co^{2+} or Ni^{2+} are formally replaced by Sr^{2+} as the structure does not contain either Co^{2+} or Ni^{2+}) we must assume that Sr vacancies at the A-site are rather adverse to the formation of $Sr_{11}Mo_4O_{23}$ (as they impede Sr substitution of Ni and/or Co). The most significant feature, however, is the extremely high amount of $Sr_{11}Mo_4O_{23}$ found in the hydrogen-reduced $Sr_2Ni_{0.5}Co_{0.5}MoO_6$ sample (~50 wt.-%). Accompanied by this high amount of $Sr_{11}Mo_4O_{23}$ is a splitting of the main peak of $Sr_2Ni_{0.5}Co_{0.5}MoO_6$ into two peaks, which can be associated with isolated $Sr_2Ni_{0.5}Co_{0.5}MoO_6$ and a single $SrMoO_3$ perovskite structure. The latter compound represents a single perovskite phase that forms in case all Ni and Co, together with 1 mol SrO and oxygen is released reductively from $Sr_2Ni_{0.5}Co_{0.5}MoO_6$. We might also anticipate that the released SrO component is partially used under reductive conditions for Co^{2+} or Ni^{2+} substitution by Sr^{2+} toward $Sr_{11}Mo_4O_{23}$. The reason why $SrMoO_3$ is observed only for $Sr_2Ni_{0.5}Co_{0.5}MoO_6$ after hydrogen reduction is the higher instability of this perovskite phase at the given chemical composition and the resulting much higher degree of decomposition, yielding a higher amount of exsolved metal particles. $Sr_2Co_{0.9}Ni_{0.1}MoO_6$, on the other hand, is chemical composition-wise much closer to the pure Sr_2CoMoO_6 and accordingly much more stable. Performing a DRM after hydrogen reduction in due course removes $Sr_{11}Mo_4O_{23}$ (as observed previously), but also leads to almost complete destruction of the remaining double perovskite structures. Only about 6 wt.-% still prevail. The rest is a large amount of $SrMoO_4$ (arising from the transformation of $Sr_{11}Mo_4O_{23}$), $SrCO_3$ and, exsolved Ni/Co particles.

A common denominator in reduction studies of Sr–Mo containing double perovskites is the product variety. Thermodynamics at low P_{O2} dictates the formation of metallic Ni and Co and a mixture of Sr_3MoO_4 and $SrMoO_4$ [43]. The former undergoes further transformation to $SrMoO_3$ and SrO. Above 1583 °C, the formation of the Sr_2MoO_4 Ruddlesden Popper type phase is observed [43]. Accordingly, the formation of $SrMoO_3$ as the most reduced Sr–Mo oxide, exclusively for the least stable $Sr_2Ni_{0.5}Co_{0.5}MoO_6$ phase, appears to be a logical conclusion based on the results of our studies conducted under the specified experimental conditions. The presence of apparently different strontium molybdate phases in our studies compared to literature-reported ones is a consequence of the different experimental conditions. As various strontium molybdates coexist within the phase diagram as a function of temperature and oxygen partial pressure, it is necessary to exercise precise control of humidity levels, as well as heating and cooling rates, in order to obtain the targeted phases [43]. For Sr_2CoMoO_6, the situation is further complicated by the possibility of Co-oxide exsolution from the double perovskite structure at low temperatures and high oxygen partial pressures, shifting the decomposition temperature of Sr_2CoMoO_6 to higher temperatures [43]. This is essentially corroborated by our results.

The exsolution of Ni and Co from the respective perovskite structures has also been followed by electron microscopy (Fig. 5). After hydrogen reduction, Sr_2NiMoO_6 shows clear signs of Ni exsolution (Panel A), with homogeneously distributed Ni particles between 10 and 50 nm. Similarly, exsolved Ni particles are also observed when Sr_2NiMoO_6 is treated in the DRM mixture directly. Ni particle sizes are comparable, but the distribution is more heterogeneous. Co exsolution from Sr_2CoMoO_6 (Panel C) after reduction in hydrogen is equally pronounced, but the morphology of exsolved Co appears more spatially extended and less particular. Extended, sometimes interconnected patches decorating the perovskite grain rims, are frequently observed. For the Ni and Co co-doped double perovskite $Sr_2Ni_{0.5}Co_{0.5}MoO_6$ we observe the exsolution of well-defined Ni–Co alloy particles in approximate sizes between 30 nm and 50 nm both if a hydrogen reduction at 800 °C is carried out prior to DRM (Panel D) or a DRM reaction is performed without hydrogen pre-reduction (Panel E). Most importantly, isolated Ni and/or Co particles are clearly underrepresented and almost exclusively, exsolved Ni–Co alloy particles have been observed in varying compositions. We have carried out on-particle EDX composition analysis for an array of particles of the $Sr_2Ni_{0.5}Co_{0.5}MoO_6$ sample after hydrogen reduction/subsequent DRM and DRM without pre-reduction and we have highlighted five of them in Panels D and E. For particles 1 and 2 in Panel D, the compositions are approximately $NiCo_{1.95}$ and $NiCo_{1.63}$, for the three particles in Panel E $NiCo_{1.5}$, $NiCo_{1.78}$ and $NiCo_{1.1}$. A statistical analysis reveals that in almost all cases, Co-richer Ni–Co alloy particles are exsolved. Furthermore, the deviation from the nominal and overall perovskite stoichiometry with respect to the Ni/Co ratio is significantly in favor of Co. The formation of Co-richer Ni–Co intermetallic nanoparticles upon exsolution is expected, as previous studies on the oxygen evolution reaction and transient oxidation of Ni–Co alloys have shown that the relative differences in the mobilities of Ni^{2+} and Co^{2+} ions lead to especially Co-richer surface regions with significant deviations from the nominal composition. This is corroborated both for the bulk and the surface by PXRD and XPS, respectively [44,45].

In conclusion, the principal findings of the PXRD and TEM experiments can be summarized as follows.

Table 3
Summary of the Rietveld-derived phases, weight fractions and lattice parameters for all samples after selected treatments.

Sample/Treatment	Phases	Weight Fraction [wt.-%]	a [Å]	b [Å]	c [Å]
Sr_2NiMoO_6	Sr_2NiMoO_6	98.9	5.5479	–	7.8957
calcined	$SrMoO_4$	1.1	5.3955	–	12.0199
Sr_2NiMoO_6	Sr_2NiMoO_6	69.7	5.5495	–	7.8976
DRM	$SrMoO_4$	13.7	5.3921	–	12.0532
	$SrCO_3$	13.6	5.1051	8.3918	6.0552
	Ni	3.0	3.5239	–	–
Sr_2NiMoO_6	Sr_2NiMoO_6	71.2	5.5494	–	7.8953
DRM second cycle	$SrMoO_4$	14.6	5.3938	–	12.0556
	$SrCO_3$	10.9	5.1064	8.4014	6.0516
	Ni	3.3	3.5254	–	–
Sr_2NiMoO_6	Sr_2NiMoO_6	67.6	5.5487	–	7.8945
H_2 treatment	$Sr_{11}Mo_4O_{23}$	22.1	16.3754	16.4369	16.4152
	Ni	10.3	3.5637	–	–
Sr_2NiMoO_6	Sr_2NiMoO_6	34.0	5.5507	–	7.8971
H_2 treatment & DRM	$SrMoO_4$	35.1	5,3921	–	12.0583
	$SrCO_3$	20.4	5.0979	8.4124	6.0477
	Ni	10.5	3.5246	–	–
Sr_2CoMoO_6	Sr_2CoMoO_6	97.4	5.5676	–	7.9533
calcined	$SrMoO_4$	2.6	5.3955	–	12.0315
Sr_2CoMoO_6	Sr_2CoMoO_6	73.5	5.5689	–	7.9506
DRM	$SrMoO_4$	13.6	5.3940	–	12.0400
	$SrCO_3$	10.3	5.1025	8.4081	6.0398
	CoO	2.7	4.2677	–	–
Sr_2CoMoO_6	Sr_2CoMoO_6	74.9	5.5724	–	7.9441
H_2 treatment	$Sr_{11}Mo_4O_{23}$	16.8	16.5118	16.4345	16.3424
	Co	8.3	3.5464	–	–
Sr_2CoMoO_6	Sr_2CoMoO_6	44.0	5.5751	–	7.9458
H_2 treatment & DRM	$SrMoO_4$	30.4	5.3903	–	12.0556
	$SrCO_3$	22.7	5.1050	8.4168	6.0429
	CoO	2.9	4.2543	–	–
$Sr_{1.9}CoMoO_6$	$Sr_{1.9}CoMoO_6$	23,7	5.5747	–	7.9385
H_2 treatment & DRM	$SrMoO_4$	43.2	5.3932	–	12.0515
	$SrCO_3$	28.7	5.1039	8.4143	6.0437
	CoO	4.3	4.2615	–	–
$Sr_2Co_{0.9}Ni_{0.1}MoO_6$	$Sr_2Co_{0.9}Ni_{0.1}MoO_6$	26.2	5.5758	–	7.9470
H_2 treatment & DRM	$SrMoO_4$	37.4	5.3905	–	12.0507
	$SrCO_3$	26.3	5.1032	8.4073	6.0398
	Co	10.1	3.5445	–	–
$Sr_2Ni_{0.5}Co_{0.5}MoO_6$	$Sr_2Ni_{0.5}Co_{0.5}MoO_6$	98.6	5.5549	–	7.9166
calcined	$SrMoO_4$	1.4	5.3905	–	12.0353
$Sr_2Ni_{0.5}Co_{0.5}MoO_6$	$Sr_2Ni_{0.5}Co_{0.5}MoO_6$	60.7	5.5405	–	7.8826
DRM	$SrMoO_4$	20.7	5.3700	–	11.9958
	$SrCO_3$	15.1	5.0738	8.3638	5.9942
	Ni/Co	3.6	3.2224	–	–
$Sr_2Ni_{0.5}Co_{0.5}MoO_6$	$Sr_2Ni_{0.5}Co_{0.5}MoO_6$	38.7	5.5460	–	7.8950
DRM second cycle	$SrMoO_4$	26.6	5.3771	–	12.0073
	$SrCO_3$	24.0	5.0904	8.3846	6.0205
	Ni/Co	10.7	3.5208	–	–
$Sr_2Ni_{0.5}Co_{0.5}MoO_6$	$Sr_2Ni_{0.5}Co_{0.5}MoO_6$	19.0	5.6103	–	8.0002
H_2 treatment	$SrMoO_3$	17.4	5.5608	–	7.9181
	$Sr_{11}Mo_4O_{23}$	51.2	16.4250	16.4654	16.4025
	Ni/Co	12.4	3.5538	–	–
$Sr_2Ni_{0.5}Co_{0.5}MoO_6$	$Sr_2Ni_{0.5}Co_{0.5}MoO_6$	6.3	5.5643	–	7.9336
H_2 treatment & DRM	$SrMoO_4$	40.1	5.3892	–	12.0552
	$SrCO_3$	39.2	5.1053	8.4112	6.0368
	Ni/Co	14.4	3.5378	–	–

- $SrMoO_4$ is formed, whenever either of the samples is annealed in the dry reforming mixture and its formation during DRM is accelerated, if a hydrogen pre-reduction is carried out.
- $SrMoO_4$ is always absent, if only a hydrogen pre-reduction is carried out.
- $Sr_{11}Mo_4O_{23}$ is formed by hydrogen reduction only and its appearance is a direct consequence of the cation-defective nature of the perovskite in reductive atmospheres due to the exsolution of Co/Ni. In less-reducing environments, such as DRM mixtures, $Sr_{11}Mo_4O_{23}$ is rapidly transformed to $SrMoO_4$.
- The formation of $SrMoO_3$ is a direct consequence of a more pronounced reductive decomposition propensity of a rather unstable double perovskite phase. A prerequisite for the formation is the rapid leaching of the B-site ions as exsolved metal particles from the perovskite structure, accompanied by the loss of SrO.
- Ni- and Co-co-doped strontium molybdate double perovskites tend to exsolve slightly Co-enriched NiCo alloy particles, but not isolated Ni and Co nanoparticles.

Phase and structure evolution during hydrogen reduction and DRM operation monitored by in situ X-ray diffraction analysis.

As we have shown in recent studies for doped single perovskites, a clear understanding of the correlation between structure and activity is only possible by in situ monitoring those changes during hydrogen reduction and DRM operation [5,8,9,50,51]. Fig. 6 shows the in situ collected PXRD patterns during a hydrogen pre-reduction treatment, followed by a DRM cycle between 25 °C and 800 °C, and Fig. 7 shows the

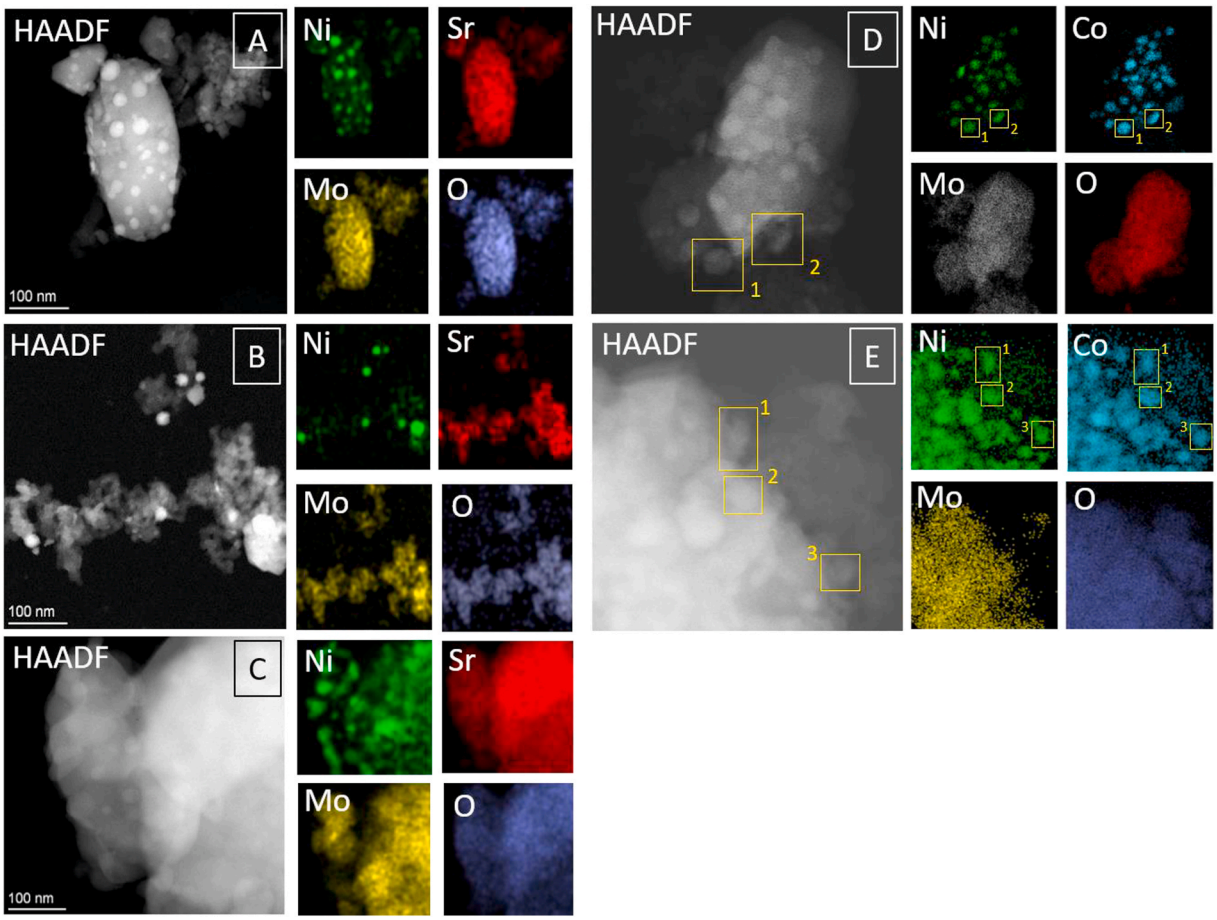

Fig. 5. HAADF-STEM and EDX analysis of Sr_2NiMoO_6 after reduction in hydrogen at 800 °C, followed by a DRM treatment up to 800 °C (Panel A), after a DRM treatment up to 800 °C without hydrogen pre-reduction (B), Sr_2CoMoO_6 after hydrogen reduction at 800 °C (Panel C), $Sr_2Ni_{0.5}Co_{0.5}MoO_6$ after a DRM treatment up to 800 °C with hydrogen pre-reduction (Panel D) and $Sr_2Ni_{0.5}Co_{0.5}MoO_6$ after a DRM treatment up to 800 °C without hydrogen pre-reduction (Panel E).

associated weight fraction analysis based on Rietveld refinement. We show the waterfall plot of the diffractograms only for Sr_2NiMoO_6, but provide for other representative samples only the weight fraction analysis (Fig. 7). The respective diffractograms are presented in summary form in the Supporting Information (Figs. S1–S3). During heating in hydrogen up to 775 °C, the double perovskite structure is remarkably stable and only above this temperature, and during the isothermal phase, the formation of the $Sr_{11}Mo_4O_{23}$ structure takes place and becomes strongly accelerated during the holding period at 800 °C. In parallel, we observe the beginning exsolution of Ni. Switching to a DRM mixture after re-cooling causes the formation of $SrMoO_4$ and $SrCO_3$ at the expense of $Sr_{11}Mo_4O_{23}$ at 500 °C. The weight fraction of Ni is essentially constant during the DRM heating up to 800 °C and also during the isothermal period at 800 °C. Decomposition of Sr_2NiMoO_6 and an associated further increase of $SrMoO_4$ and $SrCO_3$ is observed above 725 °C and during the isothermal phase of the experiment. Upon reaching the isothermal phase, the composition of the mixture reaches a steady state, which is also observed during re-cooling. If no hydrogen pre-reduction is carried out prior to DRM, hardly any changes are observed during the first DRM cycle up to 800 °C Ni exsolution, as well as formation of $SrMoO_4$ and $SrCO_3$ are only observed during the 10 min isothermal period at 800 °C. During the second DRM cycle, the multiphase mixture containing Sr_2NiMoO_6, $SrMoO_4$, Ni and $SrCO_3$ has evidently essentially reached a steady state. A slight increase in $SrMoO_4$ is observed, but again, most of the change in the composition of the sample is only observed during the isothermal period at 800 °C. If similar experiments are carried out on the Ni- and Co-co-doped material, we note a similar stability of the $Sr_2Ni_{0.5}Co_{0.5}MoO_6$ structure up to 800 °C. Some Ni exsolution is observed beginning at around 670 °C alongside the formation of $Sr_{11}Mo_4O_{23}$, which takes place between 670 °C and 800 °C. After 10 min at 800 °C, some decomposition of $Sr_2Ni_{0.5}Co_{0.5}MoO_6$ is observed (to around 90 wt.-%). A DRM treatment after the hydrogen reduction does not affect the $Sr_2Ni_{0.5}Co_{0.5}MoO_6$ very much, but rather the re-transformation of $Sr_{11}Mo_4O_{23}$ into $SrMoO_4$, accompanied by the formation of $SrCO_3$ and Ni exsolution. Surprisingly, $Sr_2Ni_{0.5}Co_{0.5}MoO_6$ appears to be less stable in a DRM mixture without hydrogen pre-reduction. Here, the partial decomposition of $Sr_2Ni_{0.5}Co_{0.5}MoO_6$ starts at around 750 °C, concurrently with the formation of additional $SrMoO_4$. After a 10 min isothermal period at 800 °C, the ratio of $SrMoO_4$, NiCo alloy and $SrCO_3$ is somewhat comparable to the state shown in Panel F after the DRM reaction, although the amount of $SrMoO_4$ appears a little bit more pronounced, as is the amount of decomposed $Sr_2Ni_{0.5}Co_{0.5}MoO_6$. It should be noted that all the Co-based Sr_2CoMoO_6 samples for the ex situ benchmark treatments in hydrogen were heated to 900 °C for the ex situ benchmark treatments in hydrogen induce the decomposition of Sr_2CoMoO_6. Hence, the pronounced formation of $Sr_{11}Mo_4O_{23}$ during hydrogen pre-reduction discussed in the context of Fig. 3 cannot be seen in the in situ experiments, as the maximum temperature was 800 °C. Nevertheless, we propose a lower threshold of 800 °C for the structural transformations under discussion. Again, the in situ PXRD data suggest that $Sr_{11}Mo_4O_{23}$ is a transient Sr-enriched Ni/Co cation-deficient phase, which is only reductively formed in the absence of CO_2 and subsequently decomposes upon SrO removal during DRM in the presence of CO_2.

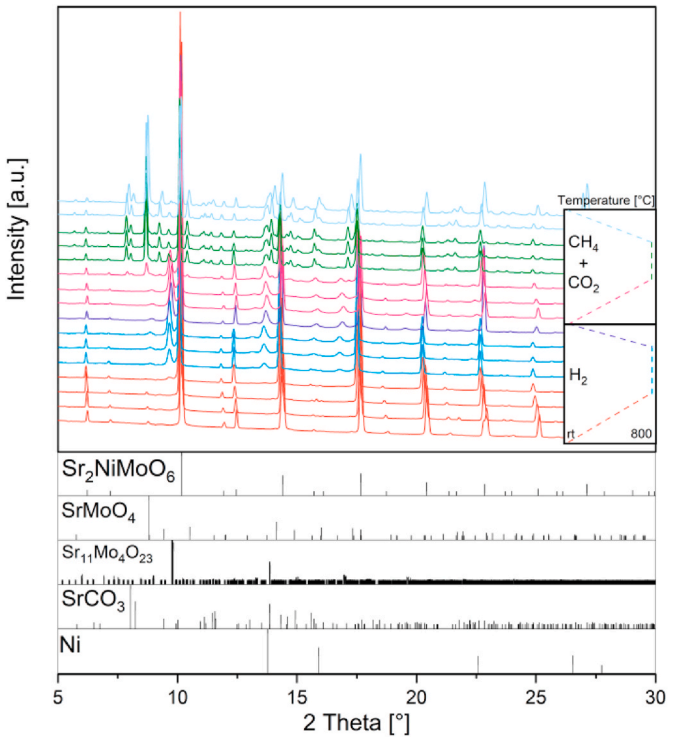

Fig. 6. In situ PXRD analysis of Sr_2NiMoO_6 for a hydrogen reduction (up to 800 °C) – DRM cycle (up to 800 °C). Hydrogen flow: 1 mL min^{-1} from 25 °C to 800 °C; DRM flow consisting of CO_2:CH_4 = 1:1, 1 mL min^{-1} from 25 °C to 800 °C. The heating program is shown as inset.

3.2.2. *Surface chemical aspects of hydrogen treatment and DRM operation*

Complementary to bulk analysis, we studied the surface chemical composition by X-ray photoelectron spectroscopy for Sr_2NiMoO_6, Sr_2CoMoO_6 and $Sr_2Ni_{0.5}Co_{0.5}MoO_6$ in the calcined state, after hydrogen reduction at 800 °C (Sr_2NiMoO_6) and 900 °C (Sr_2CoMoO_6 and $Sr_2Ni_{0.5}Co_{0.5}MoO_6$) and after direct DRM treatment up to 800 °C. The spectra are shown in Figs. 8 and 9, Tables S1 and S2 in the Supporting Information summarize the peak positions of the fitted components, their FWHM and raw area, as well as the atomic percentages. For Sr_2NiMoO_6, the untreated sample after calcination reveals the typical features for NiO, with the Ni $2p_{3/2}$ and Ni $2p_{1/2}$ peaks at 856.0 eV and 873.9 eV, alongside the two satellite peaks at 861.7 eV and 879.8 eV (topmost spectrum in Panel A) [52–56]. After the reduction in hydrogen, a second doublet feature with pronounced asymmetry, including the associated satellite peaks, typical for metallic Ni, appears at 852 eV and 869.7 eV. The respective satellites are found at 858.0 eV and 875.4 eV, respectively (middle spectrum in Panel A). After a direct DRM treatment, the same set of peaks is obtained, however, the contribution of the metallic Ni component is smaller compared to after hydrogen treatment. This is in clear agreement with the less reducing environment in DRM mixture. Overall, the Ni 2p spectra in the calcined state agree well with literature-reported spectra of Sr_2NiMoO_6 [57]. While the Sr 3d and O 1s peaks do not yield solid interpretable features, clear changes can be found for the Mo 3d peaks as a function of treatment (Panel B). Even in the calcined state, contributions of Mo^{6+} and Mo^{5+} at positions of 233.0 eV and 236.2 eV (Mo^{6+}), as well as 231.6 eV and 235.0 eV (Mo^{5+}), are observed, which indicate the presence of oxygen vacancies for the charge compensation [58–63]. After hydrogen reduction, the contribution of Mo^{5+} is diminished in favor of Mo^{4+}, resulting from Sr_2NiMoO_6 reduction. In principle, in line with the evolution of the Ni 2p peaks, no Mo^{4+} contribution is observed after DRM treatment due to the less reducing environment. The strong increase in Mo^{5+} after DRM treatment results from the defect interactions, which the DRM mechanism on perovskite structures is known for, as e.g., described in Ref. [64]. In summary, the XPS results indicate a slightly reduced Sr_2NiMoO_6 sample even after calcination with a certain amount of oxygen vacancies. The number of the latter is clearly increased both by hydrogen reduction or DRM treatment.

Sr_2CoMoO_6 exhibits the same evolution under hydrogen reduction and DRM treatment. For Sr_2CoMoO_6, the Co 2p spectrum in the calcined state represents the typical spectrum for Co^{2+} (peaks at 779.7 eV and 795.4 eV for Co $2p_{3/2}$ and Co $2p_{1/2}$, satellite peaks at 785.1 eV and 801.2 eV, Co LMM Auger transition at 772.1 eV) and is more indicative of CoO, than Co_3O_4 (topmost spectrum in Panel C) [65–69]. As for Ni 2p, Co metal is also found in surface-near regions, both after hydrogen reduction and DRM treatment, respectively. Again, the contribution of Co metal is less pronounced after a direct DRM treatment. The Mo 3d peaks follow a similar trend as those observed for Sr_2NiMoO_6, with two pronounced differences: derived from the much more pronounced Mo^{5+} intensity already after calcination, we infer a higher number of oxygen vacancies for Sr_2CoMoO_6, which after DRM give rise to a significant Mo^{4+} contribution not observed for Sr_2NiMoO_6.

Most important for the interpretation of the catalytic results in the subsequent chapter, the corresponding spectra for $Sr_2Ni_{0.5}Co_{0.5}MoO_6$ reveal a substantial difference in the Co 2p region: while the metallic Co component for Sr_2CoMoO_6 after a DRM treatment is clearly underrepresented in comparison to the oxidic component (roughly 1:10 = Co metal:Co oxidic as determined from the area ratios of the Co $2p_{3/2}$ peaks), this ratio changes to 1.5:1 = Co metal:Co oxidic for $Sr_2Ni_{0.5}Co_{0.5}MoO_6$. This indicates that co-alloying with Ni leads to a higher amount of metallic Co in the surface near regions, through the exsolution of Co-rich Ni–Co alloy nanoparticles, as evidenced by TEM (cf. Fig. 4). This presence of metallic Ni–Co states is paramount for the activation of $Sr_2Ni_{0.5}Co_{0.5}MoO_6$ during DRM (cf. Fig. 10). The Mo 3d peaks follow the same trend as Sr_2NiMoO_6 with the distinct difference that after calcination, co-doping the perovskite with Ni and Co leads to more reduced Mo species. We address this to a higher amount of oxygen vacancies. During exsolution the depletion of B-site atoms leads to the oxidation of Mo species to level again with Sr_2NiMoO_6.

3.2.3. *Carbon resilience*

We also briefly addressed the potential coking issue of all materials during DRM operation in comparison to the calcined and the hydrogen-prereduced state. Fig. S4 shows a representative set of C 1s spectra collected on $Sr_2Ni_{0.5}Co_{0.5}MoO_6$, which indicate no carbon in the calcined state (bottom spectrum) and roughly comparable, but minute amounts after hydrogen and DRM treatment (middle and top spectrum, respectively, as judged by the intensity of the graphitic carbon component at 284.6 eV. We tentatively address this suppressed coke formation by the catalytic experiments highlighted in Fig. 10: due to the high reverse water-gas shift activity and the still remaining carbon dioxide in the product mixture, the reaction-formed water is able to efficiently burn off carbon from the catalyst surface. The observed carbon signals are, thus, rather a consequence of the contact to ambient conditions after the treatments. In summary, under the chosen experimental conditions – also in line with the catalytic profiles discussed below – none of the catalysts shows significant carbon deposition or coking effects in neither electron microscopy nor XPS, despite the rather large Ni, Co or Ni–Co particles.

3.3. *Catalytic methane dry reforming performance*

Fig. 10 shows the catalytic methane dry reforming performance in a comparative fashion for Sr_2NiMoO_6, Sr_2CoMoO_6 and $Sr_2Ni_xCo_{1-x}MoO_6$. We have performed all measurements with and without a hydrogen pretreatment to trigger eventual metal exsolution and formation of a metal-perovskite heterointerface and to assess the catalytic differences upon direct treatment in a DRM mixture and DRM after a preceding

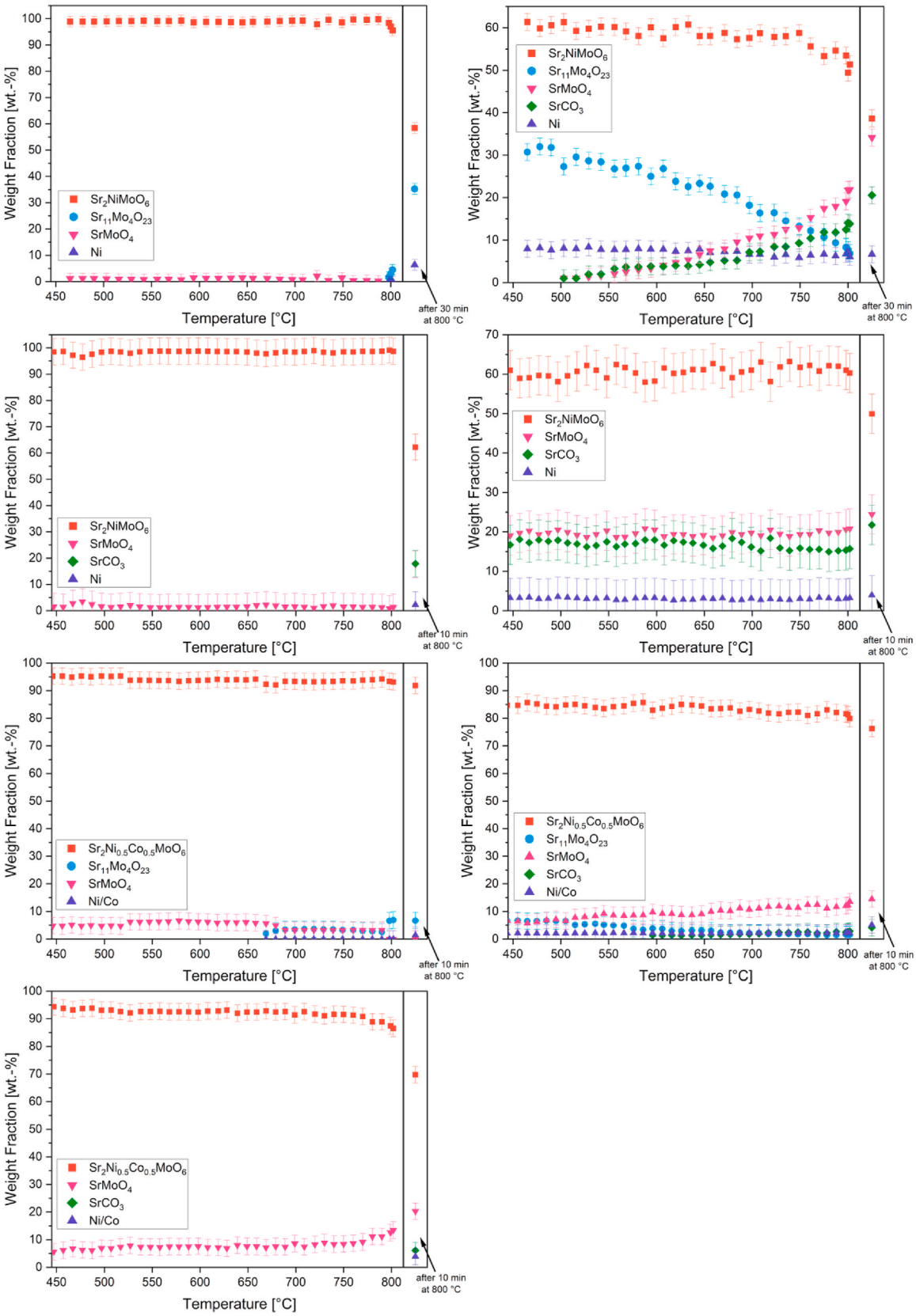

Fig. 7. Weight fraction analysis based on the Rietveld refinements of the in situ PXRD data for Sr_2NiMoO_6 and $Sr_2Ni_{0.5}Co_{0.5}MoO_6$ after different pre-reduction and DRM treatments. *Top row, left panel*: Sr_2NiMoO_6 during pre-reduction in hydrogen up to 800 °C; *Top row, right panel*: Sr_2NiMoO_6 during DRM up to 800 °C after the pre-reduction treatment is shown in the left panel. *Second-most row from the top*: Sr_2NiMoO_6 during the first (*Left Panel*) and the second DRM cycle without hydrogen pre-reduction (*Right panel*). *Second-most row from the bottom*: $Sr_2Ni_{0.5}Co_{0.5}MoO_6$ during pre-reduction in hydrogen up to 800 °C (*Left Panel*), $Sr_2Ni_{0.5}Co_{0.5}MoO_6$ during DRM up to 800 °C after the pre-reduction treatment shown in the right panel. *Bottom row*: $Sr_2Ni_{0.5}Co_{0.5}MoO_6$ during a first DRM cycle without hydrogen pre-reduction. Parameters: DRM atmosphere CO_2:CH_4 = 1:1, flow rate: 40 mL min^{-1}, heating rate: 5 °C min^{-1}.

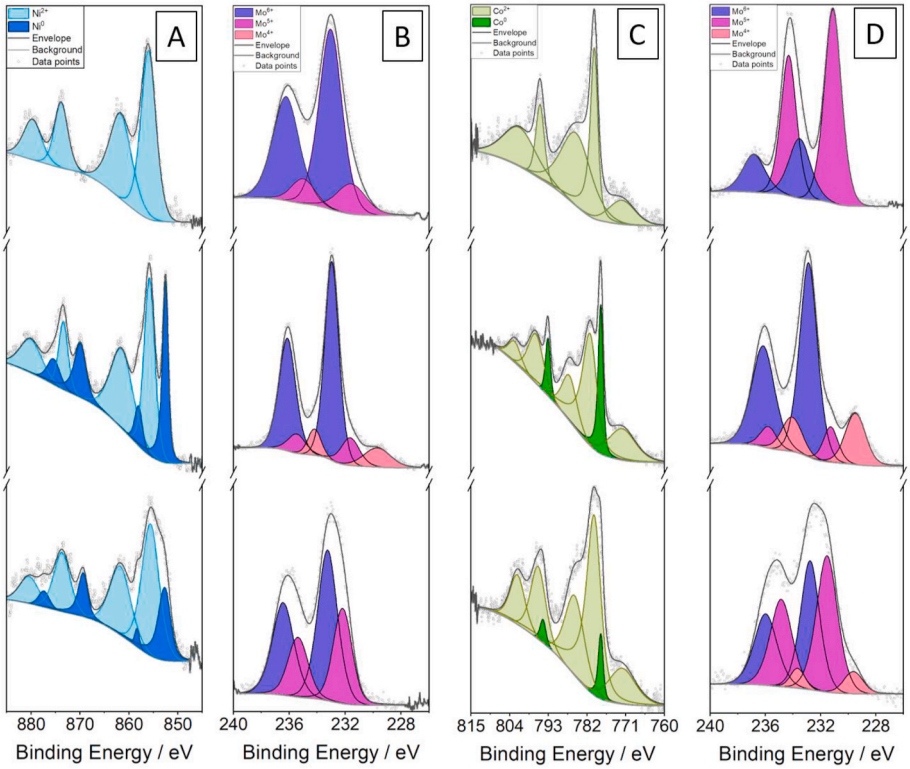

Fig. 8. Ni 2p, Co $2p_{3/2}$ and Mo 3d high-resolution XP spectra in the calcined, hydrogen-reduced and post-DRM state (from top to bottom) for Sr_2NiMoO_6 and Sr_2CoMoO_6. Panel A: Ni 2p Sr_2NiMoO_6; Panel B: Mo 3d Sr_2NiMoO_6; Panel C: Co 2p Sr_2CoMoO_6. Panel D: Mo 3d Sr_2CoMoO_6.

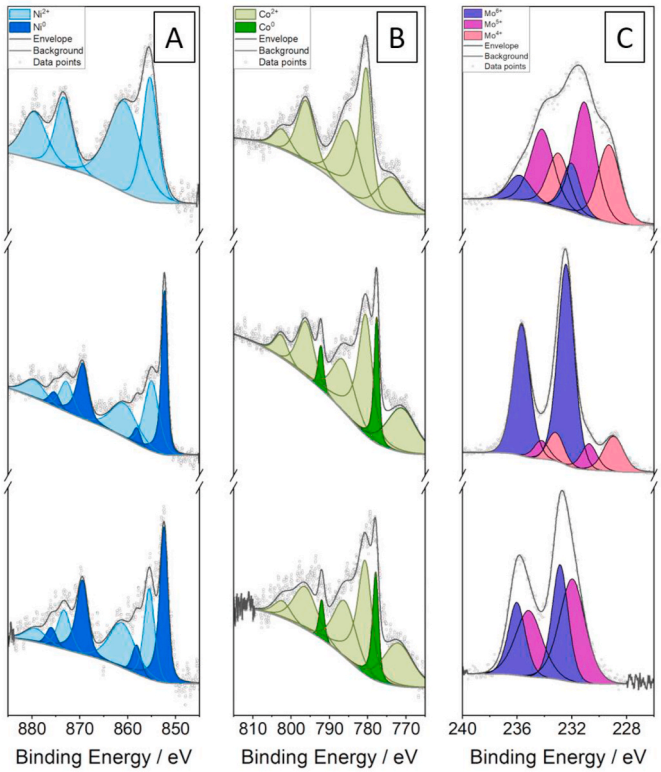

Fig. 9. Ni 2p, Co $2p_{3/2}$ and Mo 3d high-resolution XP spectra in the calcined, hydrogen-reduced and post-DRM state (from top to bottom) for $Sr_2Ni_{0.5}Co_{0.5}MoO_6$. Panel A: Ni 2p; Panel B: Co 2p; Panel C: Mo 3d.

hydrogen exposure.

Without hydrogen treatment, Sr_2NiMoO_6 reveals a steep acceleration of activity at around 795 °C during the first DRM cycle (Panel A). In the beginning, and roughly in the first minute of the isothermal section at 800 °C, the carbon dioxide and methane conversion match. After that, the carbon dioxide conversion is significantly enhanced and reaches conversion levels of ca. 85 %, while methane conversion reaches only about 55 %. The reason for this obvious deviation from stoichiometric DRM conversion is the pronounced reverse-water gas shift activity observed for Sr_2NiMoO_6. This leads to the additional formation of carbon monoxide and water and is directly reflected in the H_2/CO ratio. We observe a ratio of ~0.8 in the temperature region, where the carbon dioxide and methane traces match, indicating almost exclusive DRM activity. Above, this ratio drops to around 0.5 in line with increased reverse water gas shift activity. During the second DRM cycle, the onset of catalytic activity is markedly shifted to lower temperatures, i.e., to about 450 °C. Again, a slight deviation from stoichiometric DRM conversion of carbon dioxide and methane has been observed, saturating at conversion levels of 70 % and 50 % for carbon dioxide and methane, respectively (Panel B). If a hydrogen pre-treatment at 800 °C is carried out before the DRM test (Panel C), the onset temperature is comparable to that observed in the second DRM cycle without hydrogen pre-reduction, as are the conversion levels at 700 °C. However, a peak in the conversion is observed both for carbon dioxide and methane at around 700 °C. At higher temperatures, the conversion drops by about 10 % and subsequently approaches a constant lower level beyond 725 °C. The reason for this behavior is shown as an inset in Panel C: starting at around 650 °C, but accelerating strongly up to 800 °C, the Ni crystallite sizes more than double from 20 nm to 50 nm in the same temperature window. Hence, the decrease in catalytic conversion coincides with strong Ni crystallite sintering, which leads to an overall activity loss within the catalyst bed due to a decrease of available active Ni surface sites. This behavior is only observed for the hydrogen pre-treated sample and is somewhat also somewhat reflected in the TEM images and EDX

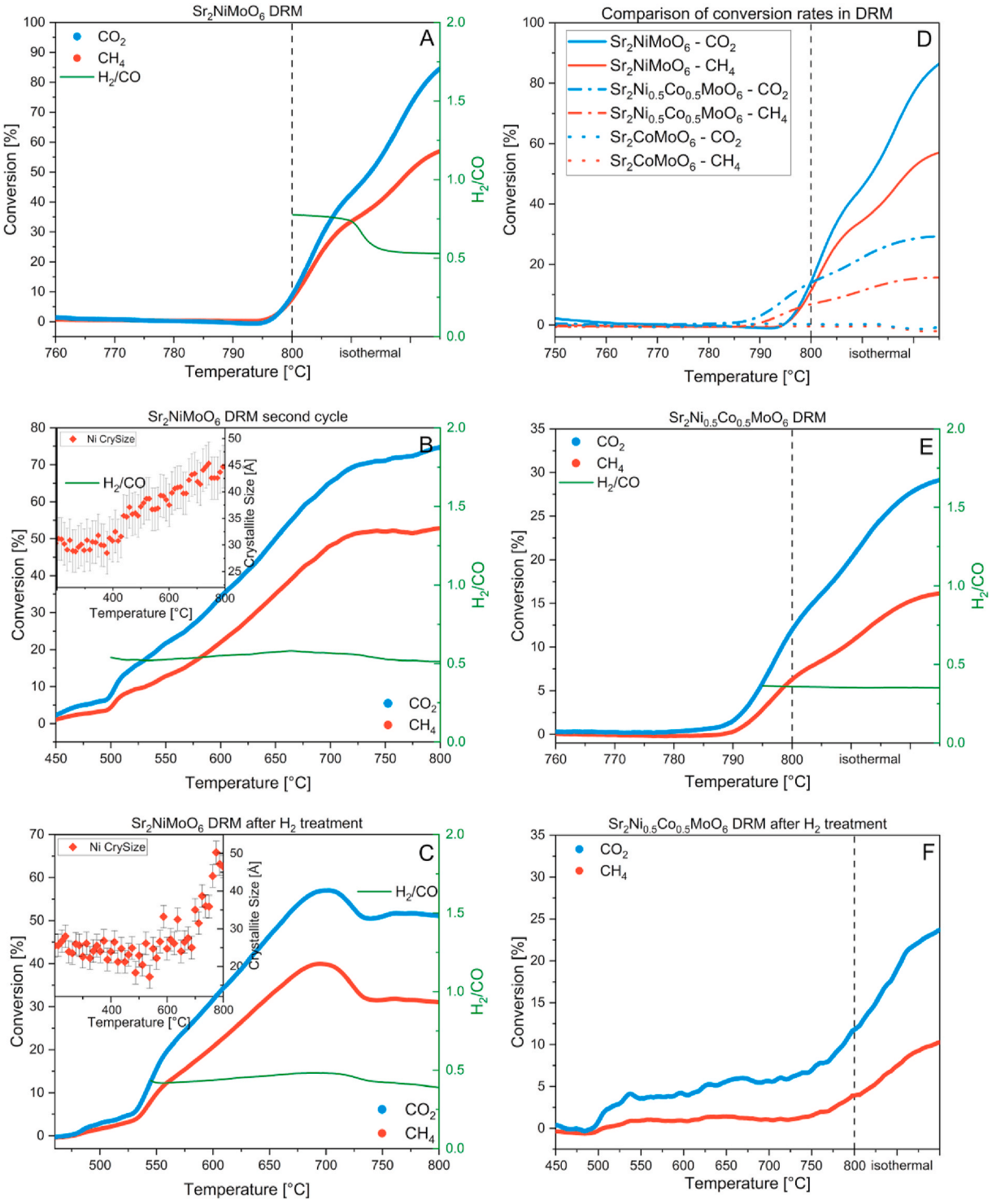

Fig. 10. Methane dry reforming performance of Sr_2NiMoO_6, Sr_2CoMoO_6 and $Sr_2Ni_xCo_{1-x}MoO_6$ after selected treatments as indicated in the individual panels. Parameters: DRM atmosphere 60 mL min^{-1} (CH_4:CO_2:He = 1:1:1 mL min^{-1}); catalyst mass: 200 mg; heating rate: 5 °C min^{-1}. Blue traces: carbon dioxide conversion, red traces: methane conversion. Isothermal sections: 10 min each. The green profiles in Panels A, B, C and E highlight the respective H_2/CO ratios (axis on the right side).

maps shown in Fig. 5. Again, the H_2/CO ratio determined at ~0.5 (Panel C, also valid for the profiles shown in Panels B and E) indicates strong contribution of the reverse water-gas shift reaction. Focussing on the DRM performance of Sr_2CoMoO_6, we at first recallthat pronounced Co metal exsolution is indeed observed after hydrogen pre-treatment at 800 °C, but hardly any is detectable after DRM up to 800 °C (Fig. 8, Panel C, middle and bottom spectra). Due to the instability/absence of Co^0 at the surface under DRM conditions, no catalytic activity is observed (Panel D). We have subsequently focussed on different activation strategies, including introducing defects at the A-site to facilitate decomposition of the perovskite (compare Fig. 3), but equally, no substantial enhancement in either Co exsolution or DRM activity was observed. In due course, we opted for Ni co-alloying, i.e., introducing different doping levels of Co with Ni to eventually increase the DRM

performance. Two different doping levels with nominal compositions $Sr_2Ni_{0.1}Co_{0.9}MoO_6$ and $Sr_2Ni_{0.5}Co_{0.5}MoO_6$ were prepared and tested. While the activity increase for the former is only minute, a pronounced activity increase was observed for the latter (Panel D, E and F). In short, the onset temperature and the behavior upon hydrogen pre-treatment and DRM performance with and without hydrogen pre-treatment are comparable to Sr_2NiMoO_6. The only pronounced difference is the overall lower maximum conversion (carbon dioxide 30 %, methane 15 % during the first DRM cycle), which can be interpreted in terms of a lower number and/or activity of mixed metallic surface sites relative to the activated Sr_2NiMoO_6 material. We, thus, conclude that the addition of Ni suppresses the oxidation propensity of Co to some extent, causing the observed activity via stabilized metallic surface sites. This is directly reflected in the XP spectra discussed in Figs. 8 and 9. Note that EDX experiments also prove that indeed Ni–Co alloy particles are primarily exsolved, and no isolated Ni and/or Co particles. By comparing the catalytic performance to similar systems described in the literature, we note that the catalytic activity in terms of conversion and H_2/CO ratio is in line with previously reported systems, e.g. in Fe-doped Sr_2NiMoO_6 materials. Carillo et al. reported exsolution of $FeNi_3$ alloy nanoparticles following a pre-reduction treatment in hydrogen for prolonged times (2–20 h) at 900 °C, which also caused partial breakdown of the parent double perovskite structure. Carbon dioxide and methane conversion levels were observed at 70–80 % and 50 % for reaction temperatures of 850 °C, respectively, with H_2/CO ratios not exceeding 0.5 [17]. Also in line with our results, the authors claimed that the competing reverse water-gas shift reaction was responsible for this phenomenon. In terms of a comparative discussion between Ni- and Co-containing double perovskites, Hossain et al. provided such measurements for different $La_2Ni(Co)MnO_6$ samples. Very high carbon dioxide and methane conversion levels were observed at 800 °C reaction temperatures for 100 h time-on-stream on La_2NiMnO_6. Also, for these systems, the carbon dioxide conversion was higher than that for methane. The purely Ni-containing materials performed consistently better compared to the purely Co-doped ones in terms of conversion and a H_2/CO ratio value of close to unity. La_2NiMnO_6 decomposes in the DRM mixture into La_2O_3, $La(OH)_3$, MnO, NiO and Ni. As for the studied La_2NiCoO_6 material, which features La_2O_3, Ni, NiO and CoO in the aged catalyst after 10 h time-on-stream, we note that separate peaks for Ni, NiO and CoO are observed, i.e. it cannot be ruled out by that study, whether the activity in La_2NiCoO_6, in fact, arises from the present Ni-containing phases, which feature a much better DRM performance [70]. Similar deactivation effects of preferred Co oxidation in Co-rich Ni–Co particles are also observed on non-perovskite catalysts, i.e., $Ce_{0.75}Zr_{0.25}O_{2-\delta}$ decorated with 3 wt.-% Ni–Co particles [71]. Table S3 summarizes the conversion performance at comparable gas hourly space velocity (GHSV) values of Sr_2NiMoO_6, $Sr_2Ni_{0.5}Co_{0.5}MoO_6$ in comparison to $LaNiO_3$, Ni/Al_2O_3 and selected literature-reported perovskite systems in DRM. CO_2 conversion levels at comparable reaction temperatures are essentially similar to or better than other Ni- and Co-containing perovskites. Compared to Ni/Al_2O_3 and $LaNiO_3$, the reverse water-gas shift activity of our materials is pronounced, and as such, is clearly dominated by the perovskite phases – as indicated by the consistently lower CH_4 conversions. As mostly also observed in the literature, the Co-containing phases feature worse than their Ni counterparts. Differences in conversion levels and catalytic activity can be mostly related to different extents of perovskite structure decomposition and the associated exsolution of Ni and/or Co particles. In contrast to most studies in literature, our Mo-based perovskites are almost exclusively structurally very stable and in most cases, the perovskite structure is at least partially retained despite exsolution effects.

With respect to structure-activity correlations, i.e., the elucidation of the direct impact of any of the dynamically formed phases on DRM activity, we note that it affects essentially three different phases, except of exsolved Ni: $SrMoO_4$, $Sr_{11}Mo_4O_{23}$ and $SrCO_3$. If we correlate the in situ XRD data with the catalytic profiles, we note that during the DRM experiment after the hydrogen pretreatment, the amount of $SrMoO_4$ essentially remains constant between 400 °C and 800 °C, although the activity onset is observed at 450 °C with a strong acceleration at higher reaction temperatures. The strong resemblance of the DRM profile after hydrogen reduction and the second DRM profile without such pre-reduction in terms of DRM onset temperature and conversion levels, as well as the constant amount of $SrMoO_4$ during the second DRM cycle, indicates that $SrMoO_4$ is merely a spectator species. The same is true for $Sr_{11}Mo_4O_{23}$. It disappears during DRM with no apparent impact on DRM activity, i.e., there is no correlation between the structural transformation of $Sr_{11}Mo_4O_{23}$ into $SrMoO_4$ and enhanced/diminished catalytic DRM activity. $SrCO_3$ appears as a reaction product of Sr phases with CO_2, but also acts as a spectator species according to in situ XRD. We therefore suspect that none of these phases without Ni exhibit DRM activity. It appears that the DRM activity is essentially driven by the exsolved Ni, Co or Ni–Co particles in possible combination with oxygen vacancies of the remaining double perovskite structure.

4. Conclusions

We have focused on a series of Sr_2MMoO_6 (M = Ni, Co and (Ni,Co)) compounds as representative model systems to highlight the capabilities of double perovskites as eventual precursor materials for methane dry reforming (DRM) applications. The key findings can be summarized as follows.

- *Stability of the double perovskite structures*: Phase-wise, pre-treatments in either pure hydrogen or dry reforming CO_2/CH_4 mixtures exclusively yield partial decomposition of the initial double perovskites through exsolution of Ni or CoO particles and the associated formation of parasitic phases, such as $SrMoO_4$ or $SrCO_3$ (in DRM mixtures).
- *Formation of the transient $Sr_{11}Mo_4O_{23}$ phase*: The formation of an oxygen-deficient and Sr-rich $Sr_{11}Mo_4O_{23}$ transient compound has been revealed by in situ powder X-ray diffraction measurements in pure hydrogen only, representing a key intermediate for double perovskite decomposition following DRM treatments.
- *Why Co-containing double perovskites are less active compared to their Ni-containing counterparts*: The main difference between the Ni- and Co-containing Sr molybdate perovskites (despite partial decomposition) is the much stronger oxidation propensity of exsolved Co, most likely by oxygen supply from the partially intact double perovskite structure and/or oxidation by the DRM gas phase. For Sr_2NiMoO_6, the resulting metallic Ni-double perovskite interface is DRM- and reverse water-gas shift active, both if a pre-reduction step in hydrogen is carried out before the DRM experiment or if Sr_2NiMoO_6 is directly decomposed in the DRM mixture.
- *Activation of Sr_2CoMoO_6*: Different strategies to improve the catalytic activity, including hydrogen by-mixing, A-site deficiency or co-alloying with Ni have been followed, but only the latter has a beneficial effect at Ni-richer compositions close to a Co:Ni = 1:1 ratio on enhancing the DRM activity. In $Sr_2Ni_{0.5}Co_{0.5}MoO_6$, the substitution of Co by Ni suppresses the oxidation behavior of Co and yields the exsolution of Co-rich Ni–Co alloy nanoparticles during DRM.
- *Influence of the B′ site cation*: We also reveal a strong response of molybdenum as the B′ site cation to reduction and DRM treatment, causing the formation of reduced Mo species accompanying the exsolution process, which can be regarded as markers of increasing oxygen anion vacancy levels.

Double perovskites structures are, therefore, perfect model systems to monitor and classify the structural and electronic interactions potentially occurring in more complex oxide-based catalyst materials, and future studies must aim at a systematic exploration of the compositional parameter space of this material class by in-situ and operando techniques to enable a more rational knowledge-based catalyst design.

CRediT authorship contribution statement

Thomas F. Winterstein: Methodology, Investigation, Formal analysis, Data curation. **Christoph Malleier:** Methodology, Investigation, Formal analysis, Data curation. **Bernhard Klötzer:** Writing – review & editing, Validation, Supervision, Conceptualization. **Volker Kahlenberg:** Writing – review & editing, Validation, Supervision, Project administration, Formal analysis, Conceptualization. **Clivia Hejny:** Writing – review & editing, Supervision, Formal analysis. **Maged F. Bekheet:** Writing – review & editing, Supervision, Formal analysis, Conceptualization. **Julian T. Müller:** Writing – review & editing, Funding acquisition. **Aleksander Gurlo:** Writing – review & editing, Funding acquisition. **Marc Heggen:** Writing – review & editing, Formal analysis, Data curation. **Simon Penner:** Writing – review & editing, Writing – original draft, Validation, Supervision, Project administration, Funding acquisition, Conceptualization.

Declaration of competing interest

The authors declare that they have no known competing financial interests or personal relationships that could have appeared to influence the work reported in this paper.

Data availability

Data will be made available on request.

Acknowledgments

The work was conducted within the framework of the Research Focus “Functional Materials” at the University of Innsbruck. This research was funded in whole or in part by the Austrian Science Fund (FWF) [P-35770-N]. For open access purposes, the author has applied a CC BY public copyright license to any author accepted manuscript version arising from this submission. The authors thank the Advanced Light Source, which is supported by the Director, Office of Science, Office of Basic Energy Sciences, of the U.S. Department of Energy under Contract No. DE-AC02- 05CH11231, and where the in situ XRD measurements were conducted at beamline 12.2.2 in the framework of the AP proposals (ALS-11921).

Appendix A. Supplementary data

Supplementary data to this article can be found online at https://doi.org/10.1016/j.mtchem.2024.102255.

References

[1] W. Jang, J. Shim, H. Kim, S. Yoo, H. Roh, A review on dry reforming of methane in aspect of catalytic properties, Catal. Today 324 (2019) 15–26, https://doi.org/10.1016/j.cattod.2018.07.032.
[2] S. Bhattar, M. Abedin, S. Kanitkar, J. Spivey, A review on dry reforming of methane over perovskite-derived catalysts, Catal. Today 365 (2021) 2–23, https://doi.org/10.1016/j.cattod.2020.10.041.
[3] F. Sharfianjazi, A. Esmaieilkhanian, L. Bazli, S. Eskanderinezhad, S. Khaksar, P. Shafiee, M. Yusuf, B. Abdullah, P. Salahshour, F. Sadegi, A review on recent advances in dry reforming of methane over Ni- and Co-based nanocatalysts, Int. J. Hydrogen Energy 47 (2022) 42213–42233, https://doi.org/10.1016/j.ijhydene.2021.11.172.
[4] N. Aramouni, J. Touma, B. Tarboush, J. Zeaiter, M. Ahmad, Catalyst design for dry reforming of methane: analysis review, Renew. Sustain. Energy Rev. 82 (2018) 2570–2585, https://doi.org/10.1016/j.rser.2017.09.076.
[5] S. Penner, PD kheyrollahi nezhad, steering the catalytic properties of intermetallic compounds and alloys in reforming reactions by controlled in situ decomposition and self-activation, ACS Catal. 11 (2021) 5271–5286, https://doi.org/10.1021/acscatal.1c00718.
[6] S. Vasala, M. Karppinen, $A_2B'B''O_6$ perovskites: a review, Prog. Solid State Chem. 43 (2015) 1–36, https://doi.org/10.1016/j.progsolidstchem.2014.08.001.
[7] X. Xu, Y. Zhong, Z. Shao, Double perovskites in catalysis, electrocatalysis and photo (electro)catalysis, Trends in Chemistry 1 (2019) 410–424, https://doi.org/10.1016/j.trechem.2019.05.006.
[8] N. Bonmassar, M.F. Bekheet, L. Schlicker, A. Gili, A. Gurlo, A. Doran, Y. Gao, M. Heggen, J. Bernardi, B. Klötzer, S. Penner, In situ-determined catalytically active state of $LaNiO_3$ in methane dry reforming, ACS Catal. 10 (2020) 1102–1112, https://doi.org/10.1021/acscatal.9b03687.
[9] M.F. Bekheet, et al., Steering the methane dry reforming reactivity of Ni/La_2O_3 catalysts by controlled in situ decomposition of doped La_2NiO_4 precursor structures, ACS Catal. 11 (2021) 43–59.
[10] N. Köpfle, et al., Zirconium-assisted activation of palladium to boost syngas production by methane dry reforming, Angew. Chem. Int. Ed. 57 (2018) 14613–14618, https://doi.org/10.1002/anie.201807463.
[11] L. Haug, et al., Zirconium carbide mediates coke-resistant methane dry reforming on nickel-zirconium catalysts, Angew. Chem. Int. Ed. 61 (2022) e202213249, https://doi.org/10.1002/anie.202213249.
[12] J. Mei, T. Liao, Z. Sun, Metal exsolution engineering on perovskites for electrocatalysis: a perspective, Mater. Today Energy 31 (2023) 101216, https://doi.org/10.1016/j.mtener.2022.101216.
[13] T. Ruh, D. Berkovec, F. Schrenk, C. Rameshan, Exsolution on perovskite oxides: morphology and anchorage of nanoparticles, Chem. Commun. 59 (2023) 3948–3956.
[14] P. Managutti, et al., Exsolution of Ni nanoparticles from A-site-deficient layered double perovskites for dry reforming of methane and as an anode material for a solid oxide fuel cell, ACS Appl. Mater. Interfaces 13 (2021) 35719–35728, https://doi.org/10.1021/acsami.1c08158.
[15] J.H. Kim, J.K. Kim, J. Liu, A. Curcio, J. Jang, I. Kim, F. Ciucci, W. Jung, Nanoparticle ex-solution for supported catalysts: materials design, mechanism and future perspectives, ACS Nano 15 (2020) 81–110, https://doi.org/10.1021/acsnano.0c07105.
[16] K. Kousi, C. Tang, I. Metcalfe, D. Neagu, Emergence and future of exsolved materials, Small 17 (2021) 2006479, https://doi.org/10.1002/smll.202006479.
[17] A. Carillo, J. Serra, Exploring the stability of Fe–Ni alloy nanoparticles exsolved from double-layered perovskites for dry reforming of methane, Catalysts 11 (2021) 741, https://doi.org/10.3390/catal11060741.
[18] Z. Du, H. Zhao, S. Yi, Q. Xia, Y. Gong, Y. Zhang, X. Cheng, Y. Li, L. Gu, K. Świerczek, High-performance anode material $Sr_2FeMo_{0.65}Ni_{0.35}O_{6-\delta}$ with in situ exsolved nanoparticle catalyst, ACS Nano 10 (2016) 8660–8669, https://doi.org/10.1021/acsnano.6b03979.
[19] Y. Wang, T. Liu, M. Li, C. Xia, B. Zhou, F. Chen, Exsolved Fe-Ni nano-particles from $Sr_2Fe_{1.3}Ni_{0.2}Mo_{0.5}O_6$ perovskite oxide as a cathode for solid oxide steam electrolysis cells, J. Mater. Chem. A 4 (2016) 14163–14169, https://doi.org/10.1039/C6TA06078A.
[20] H. Chang, H. Chen, G. Yang, J. Shi, W. Zhou, J. Bai, Y. Wang, S.D. Li, Enhanced coking resistance of Ni cermet anodes for solid oxide fuel cells based on methane on-cell reforming by a redox-stable double-perovskite $Sr_2MoFeO_{6-\delta}$, Int. J. Energy Res. 43 (2019) 2527–2537, https://doi.org/10.1002/er.4106.
[21] Y. Jiang, Y. Yang, C. Xia, H.J.M. Bouwmeester, $Sr_2Fe_{1.4}Mn_{0.1}Mo_{0.5}O_{6-\delta}$ perovskite cathode for highly efficient CO_2 electrolysis, J. Mater. Chem. A 7 (2019) 22939–22949, https://doi.org/10.1039/C9TA07689A.
[22] H. Lu, L. Lin, X. Zhang, Y. Song, H. Matsumoto, C. Zeng, N. Ta, W. Liu, D. Gao, G. Wang, et al., In situ investigation of reversible exsolution/dissolution of CoFe alloy nanoparticles in a Co-doped Sr2Fe1.5Mo0.5O6− δ cathode for CO2 electrolysis, Adv. Mater. 32 (2020) 1906193, https://doi.org/10.1002/adma.201906193.
[23] X. Meng, Y. Wang, Y. Zhao, T. Zhang, N. Yu, X. Chen, M. Miao, T. Liu, In-situ exsolution of nanoparticles from Ni substituted $Sr_2Fe_{1.5}Mo_{0.5}O_6$ perovskite oxides with different Ni doping contents, Electrochim. Acta 348 (2020) 136351, https://doi.org/10.1016/j.electacta.2020.136351.
[24] K. Zhu, T. Wu, M. Li, R. Lu, X. Zhu, W. Yang, Perovskites decorated with oxygen vacancies and Fe-Ni alloy nanoparticles as high-efficiency electrocatalysts for the oxygen evolution reaction, J. Mater. Chem. A 5 (2017) 19836–19845, https://doi.org/10.1039/C7TA05404A.
[25] H. Lu, L. Lin, X. Zhang, D. Gao, Y. Song, Y. Zhou, Q. Liu, G. Wang, X. Bao, In situ exsolved $FeNi_3$ nanoparticles on nickel doped $Sr_2Fe_{1.5}Mo_{0.5}O_{6-\delta}$ perovskite for efficient electrochemical CO_2 reduction reaction, J. Mater. Chem. A 7 (2019) 11967–11975, https://doi.org/10.1039/C9TA03065D.
[26] Y. Huang, G. Liang, M. Croft, M. Lehtimäki, M. Karppinnen, J. Goodenough, Double-perovskite anode materials Sr_2MMoO_6 (M = Co, Ni) for solid oxide fuel cells, Chem. Mater. 21 (11) (2009) 2319–2326, https://doi.org/10.1021/cm8033643.
[27] K. Momma, F. Izumi, VESTA 3 for three-dimensional visualization of crystal, volumetric and morphology data, J. Appl. Crystallogr. 44 (2011) 1272–1276.
[28] A.K. Eriksson, S.G. Eriksson, S.A. Ivanov, C.S. Knee, H. Rundlof, Phase transitions of the magnetoelectric A_2NiMoO_6 (A = Ba, Sr) and Ca_2NiWO_6 by neutron diffraction, Ferroelectrics 339 (2006) 235–243.
[29] A. Doran, L. Schlicker, C. Beavers, S. Bhat, M. Bekheet, A. Gurlo, Compact low power infrared tube furnace for in situ X-ray powder diffraction, Rev. Sci. Instrum. 88 (2017) 013903.
[30] L. Schlicker, A. Doran, P. Schneppmüller, A. Gili, M. Czasny, S. Penner, A. Gurlo, Transmission in situ and operando high temperature X-ray powder diffraction in variable gaseous environments, Rev. Sci. Instrum. 89 (2018) 033904.
[31] DIFFRAC. TOPAS 5.0, Bruker 2024.
[32] L. Haug, et al., A laboratory-based multifunctional near ambient pressure X-ray photoelectron spectroscopy system for electrochemical, catalytic, and cryogenic studies, Rev.Sci. Instr. 94 (2023) 065104.
[33] A. Aguadero, J.A. Alonso, R. Martinez-Coronado, M.J. Martinez-Lope, M. T. Fernandez-Diaz, Evaluation of Sr_2CoMoO_{6-x} as anode material in solid-oxide fuel cells: a neutron diffraction study, J. Appl. Phys. 109 (2011) 034907.

[34] I.C. Nogueira, L.S. Cavalcante, P.F.S. Pereira, M.M. de Jesus, J.M. Rivas Mercury, N.C. Batista, M. Siu Li, E. Longo, Rietveld refinement, morphology and optical properties of $(Ba_{1-x}Sr_x)MoO_4$ crystals, J. Appl. Crystallogr. 46 (2013) 1434–1446.
[35] S.M. Antao, I. Hassan, The orthorhombic structure of $CaCO_3$, $SrCO_3$, $PbCO_3$ and $BaCO_3$: linear structure trends, Can. Mineral. 47 (2009) 1245–1255.
[36] C. Miranda, D. Villarroel-Rocha, K. Sapag, C. Alberto Lopez, J. Carmelo Pedregosa, J. Alonso, Synthesis conditions impact on $Sr_{11}MoO_4O_{23}$ electroceramic: crystal structure, stability and transport properties, RSC Adv. 11 (2021) 13814–13820.
[37] J.O. Conway, T.J. Prior, Interstitial nitrides revisited – a simple synthesis of M_xMo_3N (M = Fe, Co, Ni), J. Alloys Compd. 774 (2019) 69–74.
[38] A. Khort, S. Roslyakov, P. Loginov, Solution combustion synthesis of single-phase bimetallic nanomaterials, Nano-Structures and Nano Objects 26 (2021) 100727.
[39] S. Sasaki, K. Fujino, Y. Takeuchi, X-ray determination of electron-density distributions in oxides, MgO, MnO, CoO, and NiO, and atomic scattering factors of their constituent atoms, Proc. Japan Acad. 55 Ser. B 21 (1979) 43–48.
[40] L. Skutina, E. Filonova, D. Medvedev, A. Maignan, Undoped Sr_2MMoO_6 Double perovskite molybdates (M=Ni, Mg, Fe) as promising anode materials for solid oxide fuel cells, Materials 14 (2021) 1715.
[41] M.A. Gwan, J.W. Yun, Carbon Tolerance effects of Sr_2NiMoO_{6-d} as an alternative anode in solid oxide fuel cell under methane fuel condition, J. Eur. Ceram. Soc. 36 (2016) 1–16.
[42] L. Dos Santos-Gomez, L. Leon-Reina, J.M. Porras-Vasquez, E.R. Losilla, D. Marrero-Lopez, Chemical stability and compatibiliity of double perovskite anode materials for SOFCs, Solid State Ionics 239 (2013) 1–7.
[43] V.V. Sereda, D.S. Tsvetkov, A.L. Sednev, A.I. Druzhinina, D.A. Malyshkin, A. Yu Zuev, Thermodynamics of Sr_2NiMoO_6 and Sr_2CoMoO_6 and their stability under reducing conditions, Phys. Chem. Chem. Phys. 20 (2018) 20108–20116.
[44] M.C. Viola, M.J. Martinez-Lopez, J.A. Alonso, P. Velasco, J.L. Martinez, J. C. Pedregosa, R.E. Carbonio, M.T. Fernandez-diaz, Induction of colossal magnetoresistance in the double perovskite Sr_2CoMoO_6, Chem. Mater. 14 (2002) 812–818.
[45] C. Graves, B.R. Sudireddy, M. Mogensen, Molybdate based ceramic negative electrode materials for solid oxide cells, ECS Trans. 28 (2010), 1773-192.
[46] S. Vasala, M. Lehtimäki, Y.H. Huang, H. Yamauchi, J.B. Goodenough, M. Karppinen, Egree of order and redox balance in B-site ordered double-perovskite oxides, $Sr_2MMoO_{6-\delta}$ (M=Mg, Mn, Fe, Co, Ni, Zn), J. Solid State Chem. 183 (2010) 1007–1012.
[47] K. Zheng, K. Swierczek, Physicochemical properties of rock salt-type ordered Sr_2MMoO_6 (M= Mg, Mn, Fe, Co, Ni) double perovskites, J. Eur. Ceram. Soc. 34 (2014) 4273–4284.
[48] T. Wei, Y. Li, X. Meng, Y. Zhang, $Sr_2NiMoO_{6-\delta}$ as anode material for $LaGaO_3$-based solid oxide fuel cell, Electrochem. Commun. 10 (2008) 1369–1372.
[49] K. Zheng, K. Swierczek, W. Zajac, A. Klimkowicz, Rock salt ordered-type double perovskite anode materials for solid oxide fuel cells, Solid State Ionics 257 (2014) 9–16.
[50] P.D.K. Nezhad, et al., Elucidating the role of earth alkaline doping in perovskite-based methane dry reforming catalysts, Catal. Sci. Technol. 12 (2022) 1229–1244.
[51] P.D.K. Nezhad, et al., Mechanistic in situ insights into the formation, structural and catalytic aspects of the La_2NiO_4 intermediate phase in the dry reforming of methane over Ni-based perovskite catalysts, Appl. Catal., A 612 (2021) 117984.
[52] K.K. Lian, D.W. Kirk, S.J. Thorpe, Investigation of a "Two-State" tafel phenomenon for the oxygen evolution reaction on an amorphous Ni-Co alloy, J. Electrochem. Soc. 142 (1995) 3704–37712.
[53] G.C. Wood, B. Chattopadhyay, Transient oxidation of Ni-base alloys, Corrosion Sci. 10 (1970) 471–480.
[54] C.L. Bianchi, M.G. Cattania, P. Villa, XPS characterization of Ni and Mo oxides before and after “in situ” treatments, Appl. Surf. Sci. 70/71 (1993) 211–216.
[55] A.P. Grosvenor, M.C. Biesinger, R. Smart, N. McIntyre, New interpretations of XPS spectra of nickel metal and oxides, Surf. Sci. 600 (2006) 1771–1779.
[56] C.E. Dube, B. Workie, S.P. Kounaves, A. Robbat Jr., M. Aksub, G. Davier, Electrodeposition of metal alloy and mixed oxide films using a single-precursor tetranuclear copper-nickel complex, J. Electrochem. Soc. 142 (1995) 3357–3365.
[57] L. Xu, Y. Wan, H. Xie, Y. Huang, L. Yang, L. Qin, H. Seo, Synthesis, surface structure and optical properties of double perovskite Sr_2NiMoO_6 nanoparticles, Appl. Surf. Sci. 389 (2016) 849–857.
[58] J.F. Moulder, W.F. Stickle, P.E. Sobol, K.D. Bomben, Handbook of X-Ray Photoelectron Spectroscopy, Perkin-Elmer Corporation, Eden Prairie, Minnesota 55344, United States of America, 1992.
[59] N. Fairley, V. Fernandez, M. Richard-Plouet, C. Guillot-Deudon, J. Walton, E. Smith, D. Flahaut, M. Greiner, M. Biesinger, S. Tougaard, D. Morgan, J. Baltrusaitis, Systematic and collaborative approach to problem solving using X-ray photoelectron spectroscopy, Appl. Surf. Sci. Adv. 5 (2021) 100112.
[60] J.E. Devries, H.C. Yao, R.J. Baird, H.S. Ghandi, Characterization of molybdenum-platinum catalysts supported on y-alumina by X-ray photoelectron spectroscopy, J. Catal. 84 (1983) 8–14.
[61] T.I. Koranyi, I. Manninger, Z. Paal, O. Marks, J.R. Guenter, Activation of unsupported CO-mo catalysts in thiophene hydrodesulfurization, J. Catal. 116 (1989) 422–439.
[62] N.S. McIntyre, D.D. Johnston, L.L. Coatsworth, R.D. Davidson, J.R. Brown, X-Ray photoelectron spectroscopic studies of thin film oxides of cobalt and molybdenum, Surf. Interface Anal. 15 (1990) 26S272.
[63] L. Benoist, D. Gonbeau, G. Pfister-Guillouzo, E. Schmidt, G. Meunier, A. Levasseur, XPS analysis of lithium intercalation in thin films of molybdenum oxysulphides, Surf. Interface Anal. 22 (1994) 206–210.
[64] S. Das, S. Bhattar, L. Liu, Z. Wang, S. Xi, J.J. Spivey, S. Kawi, Effect of partial Fe substitution in $La_{0.9}Sr_{0.1}NiO_3$ perovskite-derived catalysts on the reaction mechanism of methane dry reforming, ACS Catal. 10 (2020) 12466–12486.
[65] M. Anwar, C.A. Hogarth, R. Bulpett, Effect of substrate temperature and film thickness on the surface structure of some thin amorphous films of MoO_3 studied by X-ray photoelectron spectroscopy (ESCA), J. Mater. Sci. 24 (1989) 3087–3090.
[66] A.G. Kochur, A.T. Kozakov, K.A. Googlev, A.S. Mikheykin, V.I. Torgashev, A. A. Bush, A.V. Nikolskii, Chemical bonding and valence state of 3d-metal ions in $Ni_{1-x}Co_xCr_2O_4$ spinels from X-ray diffraction and X-ray photoelectron spectroscopy data, J. Electron. Spectrosc. Relat. Phenom. 195 (2014) 208–219.
[67] B. Jit Tan, K.J. Klabunde, P.M.A. Sherwood, XPS studies of solvated metal atom dispersed catalysts. Evidence for layered cobalt-manganese particles on alumina and silica, J. Am. Chem. Soc. 113 (1991) 855–861.
[68] M.C. Biesinger, B.P. Payne, A.P. Grosvenor, L.W.M. Lau, A.R. Gerson, R. Smart, Resolving surface chemical states in XPS analysis of first row transition metals, oxides and hydroxides: Cr, Mn, Fe, Co and Ni, Appl. Surf. Sci. 257 (2011) 2717–2730.
[69] A.V. Naumkin, T.M. Ivanova, A.V. Shchukarev, A.A. Sidorov, M.A. Kiskin, I. L. Eremenko, X-Ray photoelectron spectra of cobalt trimethylacetates, Dokl. Chem. 411 (2006) 234–239, https://doi.org/10.1134/S0012500806120044.
[70] A. Hossain, M. Bhattacharjee, K. Ghorai, J. Llorca, M. Vasundhara, S. Roy, P. Bera, M. Seikh, A. Gayen, High activity in the dry reforming of methane using a thermally switchable double perovskite and in situ generated molecular level nanocomposite, Phys. Chem. Chem. Phys. 26 (2024) 5447–5465.
[71] M.A. Vasiliades, C.M. Damaskinos, P. Djinovic, A. Pintar, A.M. Efstathiou, Dry reforming of CH4 over $NiCo/Ce_{0.75}Zr_{0.25}O_{2-\delta}$: the effect of Co on the site activity and carbon pathways studied by transient techniques, Catal. Commun. 149 (2021) 106237.